Vertical mixing in the Arctic Ocean inferred from eXpendable Current Profilers

Anja Kristiansen Meyer

May 31, 2011

UNIVERSITY OF BERGEN
GEOPHYSICAL INSTITUTE

Acknowledgements

First of all I would like to thank my supervisor Professor Ilker Fer for the opportunity to work on this very interesting master thesis. Further, for funding my visit to the Polar Science Center at the University of Washington and for all his support during the last two years. His guidance and time invested in this project has been deeply appreciated.

I would like to thank the Polar Science Center for making the XCP data available to use in this thesis. Specifically Dr. James H. Morison for his warm welcome. His hospitality made the stay both educational and fun. I am very grateful.

To Roger Andersen for recovering the XCP data during my visit to the Polar Science Center and letting me contribute when possible, and for information about technical issues concerning the instrument and processing.

Further thanks go to everyone involved in my visit to Seattle. For making my stay so pleasurable and interesting in more ways I could have hoped for.

Finally, and perhaps most importantly, I would like to thank my fellow students at GFI for making the last five years of my life the most memorable thus far.

Anja Kristiansen Meyer
Bergen, May 31, 2011

Abstract

Recent and historical data sets from different regions of the Arctic Ocean are analysed using velocity profiles from 127 eXpendable Current Profiler (XCP) deployments from the time period 1993 to 2010. The data sets are processed identically. The shear profiles of horizontal velocity are used to infer vertical mixing. Using the fine-scale parameterization which relate internal wave energy to energy dissipation rate, the diapycnal eddy diffusivity is inferred. An improved version of the fine-scale parameterization which includes corrections for the shear-strain ratio and variation in latitude is also employed. Joint microstructure measurements made it possible to compare the XCP derived eddy diffusivity with direct observations to test the applicability of the parameterization. It is concluded that the skill of the XCP derived eddy diffusivity in the Arctic Ocean is within a factor of 5-6. Using XCP deployments done at the same time and same location the accuracy of the eddy diffusivity calculation is estimated to be within one order of magnitude. The eddy diffusivity values are compared in relation to topographic variations and temporal variability. For the deeper layers of the ocean, the eddy diffusivity values averaged for slope and ridge areas are comparable, and a factor of two higher than those for the abyss. The analysis on the temporal variability was inconclusive due to relatively poor quality data set from 1993.

Contents

Chapter 1

Introduction

The Arctic Ocean is an important part of the climate system and the World ocean circulation due to its interaction with the Atlantic and the Pacific Oceans through Fram and Bering Straits (see section (3.1) for place names). Water from the Arctic Ocean contributes to the deep water formation and hence also to the thermohaline circulation (Aagaard et al. 1985). In present climate, the Arctic Ocean is partially covered with ice. A change in climate, however, can cause a retreat in the ice cover, which will have consequences for both the atmosphere and ocean circulation. This will involve changes in the surface air temperature, radiative fluxes, and ocean conditions and currents (Serreze et al. 2007). A retreat in the Arctic ice cover will also change the albedo in the Arctic, as snow-covered sea ice and bare sea ice reflects more incoming solar radiation than open water. Consequently, more solar heat will be absorbed in the Arctic Ocean, which will affect the remaining ice cover and ice growth (Perovich et al. 2008).

The Arctic ice cover is maintained by a delicate balance where ocean mixing is important through the magnitude and distribution of the vertical heat flux (Fer 2009). An annual average heat flux of about 2 Wm^{-2} at the ice undersurface is required to maintain the observed thickness of perennial ice (Maykut & Untersteiner 1971, Maykut 1982) and a source of heat can be found in the Atlantic Water circulating in the Arctic Ocean.

The ocean surface and the overlaying ice-cover is currently separated from the warm Atlantic Water below by the cold halocline layer (CHL). This is a strongly stratified layer, with the change in density dominated by the increase in salinity (Aagaard et al. 1981, Rudels et al. 1996). Steele & Boyd (1998) show from data collected in spring 1995 during the Scientific Ice Expedition (SCICEX'95) that the CHL retreated throughout much of the Eurasian Basin, leaving the surface winter mixed layer in direct contact with the Atlantic Water. Follow-up surveys, however, showed that the CHL recovered (Boyd et al.

2002). The CHL is maintained by a weak turbulent diffusion, and can be destroyed by vertical mixing rates of about 5×10^{-5} $m^2 s^{-1}$ (Fer 2009). This amount of mixing can likely be achieved in an ice-free Arctic when the ice cap no longer shelters the upper layers from wind forcing. Internal waves can be generated by perturbations in the ocean stratification and contain energy which is made available for mixing when they break. These perturbations can come from atmospheric forcing like wind. But when sea-ice is present, even strong storms do not make a significant difference (Pinkel 2005). Due to the ice-cover, the internal wave field in the Arctic is less energetic compared to mid-latitudes (Levine et al. 1985, D'Asaro & Morison 1992). Rainville & Woodgate (2009), using moored measurements on shelf, find that the energy in the low frequency band affected by the Earth's rotation (i.e. near-inertial energy) is elevated in the absence of ice. They suggest that internal waves and wind forcing can become more important, leading to enhanced mixing and a change in the heat storage in the upper layer of the ocean.

Zhang & Steele (2007) used an ice-ocean model to investigate the sensitivity of the circulation of Atlantic Water in the Arctic Ocean to vertical mixing. The results show that varying the vertical mixing leads to a change in the ocean stratification and the structure of the CHL. In the Canada and Makarov Basins the changes are large enough to change the direction of the circulation in the Atlantic Water layer. Strong vertical mixing weakens the ocean stratification and results in an anticyclonic circulation at all depths. Weak vertical mixing makes the ocean unrealistically stratified with the upper layer of the ocean being fresher than observations, resulting in a strong anticyclonic circulation in the upper layer and cyclonic circulation in a shallow underlying layer.

In this Master's study, it is hypothesized that the presence of an ice cover in the Arctic Ocean results in a less energetic internal wave field and that a seasonally ice-free Arctic can lead to an increased internal wave activity and enhanced vertical mixing which can remove the CHL. Recent and historical data from different regions of the Arctic Ocean, acquired by the eXpendable Current Profilers (XCP), are analysed. The XCP infers profiles of temperature and horizontal velocity relative to a depth independent mean (Sanford et al. 1982).

A part of this study involved visiting the Polar Science Center at the University of Washington for data mining. Available historical XCP data from the Arctic are revived. Together with recent XCP data collected by a collaborative effort between the Geophysical Institute, University of Bergen and Polar Science Center, University of Washington, a study on mixing in the Arctic Ocean can be conducted using all the XCP data processed

in the same way. The XCP data provided by the Polar Science Center is available at $http://psc.apl.washington.edu/northpole/Mixing.html$.

Vertical mixing is inferred from fine-scale parameterization, Gregg (1989), using internal wave energy. The internal wave energy is inferred from shear profiles. The results are compared in relation to topographic variations, from slope areas, ridges and away from topography. As D'Asaro & Morison (1992) noted, a correlation between bottom topography and internal wave shear is expected with elevated mixing over rough bottom topography. The possible role of changing ice cover on increasing the internal wave energy in the Arctic, and the temporal variability are addressed using surveys covering from 1993 to 2010.

Theory and methods are presented in chapter 2, with a focus on internal waves in the Arctic and the parameterization used in this study. Chapter 3 introduces the data set used in this study together with information about the XCP processing. Results and discussion are presented in chapters 4 and 5.

Chapter 2

Theory and methods

2.1 Internal waves

Internal waves are common in the ocean interior, and can be observed as vertical displacement of constant density or temperature surfaces. Compared to the surface waves, the periods of the shortest internal waves are greater and their speeds are slower. Amplitudes of these short internal waves can vary between centimetres and tens of meters. Internal waves propagate both vertical and horizontal, unlike surface waves which only propagate horizontally. The signature of the internal waves on the ocean surface is small.

The internal wave frequencies are bounded by the horizontal inertial frequency $f = 2\Omega \sin(\Phi)$, where Ω is the Earth's rate of rotation and Φ is the latitude, and the vertical buoyancy frequency $N^2 = -\frac{g}{\rho}\frac{\partial \rho}{\partial z}$, where g is the acceleration due to gravity, ρ is the ocean density and z is the vertical distance. Starting with the equation of motion and the continuity equation, the angle of the wavenumber vector $\mathbf{k}$ inclined to the horizontal can be found (Munk 1981). Neglecting friction and viscosity, applying the Boussinesq approximation, linearizing the equations, assuming incompressibility and $w = w(z) \exp i(kx - \omega t)$, the equations are reduced to

$$\frac{d^2\xi}{dz^2} + k^2 \frac{N^2(z) - \omega^2}{\omega^2 - f^2}\xi = 0 \tag{2.1}$$

where $\xi = \int w dt$ is the vertical displacement and ω is the internal wave frequency. In a continuously stratified ocean with constant N, the solution to Eq. (2.1) is

$$\xi(z) = a \sin mz, \qquad m^2 = k^2 \frac{N^2 - \omega^2}{\omega^2 - f^2} \tag{2.2}$$

where a is a constant and m and k are the vertical and horizontal wavenumber components, which gives the dispersion relation (i.e. the frequency depends on the wavenumber) when solved for ω^2

$$\omega_j^2 = \frac{k^2 N^2 + m_j^2 f^2}{m_j^2 + k^2}, \qquad m_j H = j\pi, \quad j = 1, 2, ... \tag{2.3}$$

where H is the total water depth and j is the different modes. From Eq. (2.2) the angle of wave propagation (θ) for internal waves is described as

$$\tan\,\theta = \frac{m}{k} = \left(\frac{N^2 - \omega^2}{\omega^2 - f^2}\right)^{1/2} \tag{2.4}$$

For near inertial waves, i.e. internal waves with $\backsim f$ frequency, this angle is large, and for high frequency waves very small, see figure (2.1).

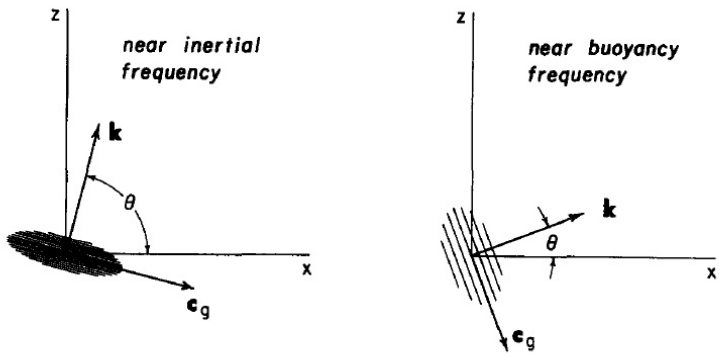

Figure 2.1: An illustration of the wavenumber vector $\mathbf{k} = (k, m)$ and group velocity c_g for the near inertial frequency and buoyancy frequency respectively (Munk 1981).

For inertial waves, particles move in horizontal orbits, and for waves with $\omega = N$, in orbits along the z-axis, in the same direction as the group velocity. The angle from the

horizontal at which the internal wave energy travels is given by

$$\tan\, c = \tan\left(90^\circ - \theta\right) = \left(\frac{\omega^2 - f^2}{N^2 - \omega^2}\right)^{1/2} \tag{2.5}$$

When the internal wave energy reaches the bottom slope, it can forward reflect, back reflect, or dissipate where it reaches the bottom. If the inclination of the bottom slope is γ, forward reflection happens when $\gamma/c < 1$ (sub-critial slope). $\gamma/c > 1$ leads to reflection back into the ocean interior and $\gamma/c = 1$ (critical slope) leads to reflection of the coming wave itself, resulting in non-linear interaction and dissipation of energy and mixing near the bottom, see figure (2.2)

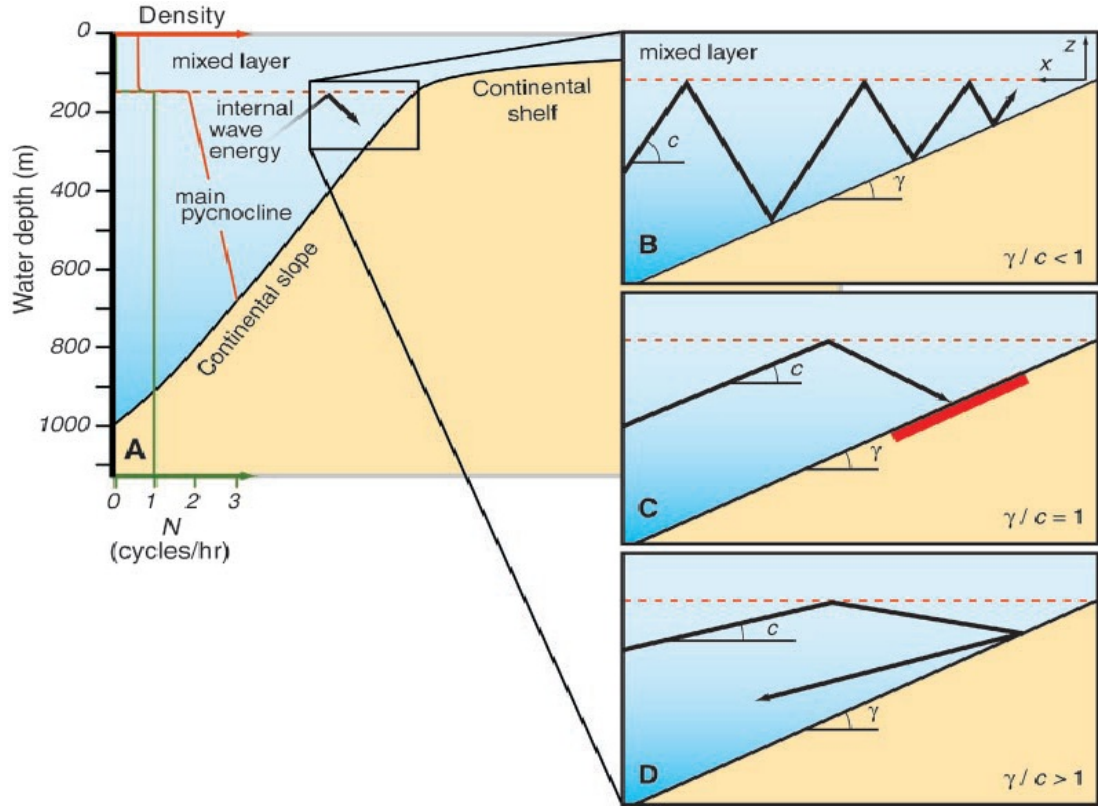

Figure 2.2: Panel (a) shows a simplified density profile (red) and the buoyancy frequency profile (green). When the internal wave energy encounters the bottom slope, with the angle of propagation c and the angle of the bottom slope γ to the horizontal, (b) the energy will forward reflect when $\gamma/c < 1$, (c) dissipate and contribute to mixing where it reaches the bottom when $\gamma/c = 1$ (critical slope) or (d) reflect back into the ocean interior when $\gamma/c > 1$ (Cacchione et al. 2002).

Because the linear internal waves cannot have frequencies less than f, and because f

increases with latitude, near-inertial waves can only travel equatorward. In the Arctic the near-inertial waves will be refracted towards the ocean boundaries, where they potentially contribute to mixing.

2.2 Garrett and Munk internal wave spectra

Garrett & Munk (1972) presented, based on observations, an empirical model spectrum of the internal wave field. Isotropy in the horizontal and being away from boundaries are assumed. The model has been revised through the years. Here Garrett & Munk (1975), modified by Cairns & Williams (1976), referred to as GM76 hereafter, is used. The Arctic Ocean is a geographical region where the internal wave field deviates from this spectrum (Levine et al. 1985, Fer et al. 2010).

In the GM76 as presented by Gregg & Kunze (1991) the vertical wavenumber spectra of the vertical isopycnal displacement, ζ, and the horizontal velocity, $V = u + iv$ are given as

$$\Phi_\zeta(\beta) = \frac{E_{GM} b^3}{2\pi j_*} \left(\frac{N_0}{N}\right)^2 \frac{1}{(1+\beta/\beta_*)^2} \qquad \left[\frac{\mathrm{m}^2}{\mathrm{radm}^{-1}}\right] \tag{2.6}$$

$$\Phi_V(\beta) = \frac{3E_{GM} b^3}{2\pi j_*} N_0^2 \frac{1}{(1+\beta/\beta_*)^2} \qquad \left[\frac{\mathrm{m}^2\mathrm{s}^{-2}}{\mathrm{radm}^{-1}}\right] \tag{2.7}$$

where $E_{GM} = 6.3 \times 10^{-5}$ is the non-dimensional energy level, $N_0 = 5.24 \times 10^3 \mathrm{s}^{-1}$, $\beta = ((\pi j)/b)(N/N_0)$ is the vertical wavenumber, j is the mode number, $j_* = 3$ is the reference mode number for GM76 and $\beta_* = ((\pi j_*)/b)(N/N_0)$ is the reference vertical wavenumber. The vertical wavenumber spectra of vertical strain and shear can be given as

$$\Phi_{\zeta_z}(\beta) = \beta^2 \Phi_\zeta(\beta) \qquad \left[\frac{1}{\mathrm{radm}^{-1}}\right] \tag{2.8}$$

$$\Phi_{V_z}(\beta) = \beta^2 \Phi_V(\beta) \qquad \left[\frac{\mathrm{s}^{-2}}{\mathrm{radm}^{-1}}\right] \tag{2.9}$$

where $\zeta_z = \partial\zeta/\partial z$ is the vertical derivative of isopycnal displacement (strain) and $V_z = u_z + iv_z$ is the shear with u and v being the horizontal velocity components. By integrating the spectra in Eqs. (2.6) and (2.7) to an upper cutoff wavenumber β_u, the total variances of strain and shear are

$$\langle \xi_z^2 \rangle = \frac{\pi E_{GM} b j_* \beta_u}{2} \qquad [-] \tag{2.10}$$

$$\langle V_z^2 \rangle = \frac{3\pi E_{GM} b j_* N^2 \beta_u}{2} \left(\frac{N}{N_0^2} \right) \qquad [\mathrm{s}^{-2}] \tag{2.11}$$

where $\langle ... \rangle$ denotes averaging. The typical upper cutoff wavenumber is $\beta_u = 2\pi/\ 10$ m $= 0.6$ rad m^{-1}, (i.e. 0.1 cycles per meter, cpm). For $\beta_u = 0.6$ rad m^{-1}, $\langle \xi_z^2 \rangle = 0.23$ and

$$\langle V_z^2 \rangle = 1.91 \times 10^{-5} \left(\frac{N}{N_0^2} \right) \qquad [\mathrm{s}^{-2}] \tag{2.12}$$

2.3 Spectral analysis

Spectral analysis can be used to find out how much the variance of for example the horizontal velocity is associated with a particular wavenumber or frequency band. Power spectral density can be generated using the fast Fourier transform (see e.g. Emery & Thomson (1997)). For a discrete sample $y(n)$ the data are transformed directly to obtain the Fourier components $Y(f)$ using Eq. (2.13).

$$Y_k = \Delta t \sum_{n=1}^{N} y_n e^{-i2\pi f_k n \Delta t}, \quad f_k = k/N\Delta t, \quad k = 0, ..., N \tag{2.13}$$

where f_k are the frequencies confined to the Nyquist interval when $-\dfrac{1}{2\Delta t} \leq f \leq \dfrac{1}{2\Delta t}$. A two- sided power spectral density is then

$$
\begin{aligned}
S_{yy}(0) &= \frac{1}{(N+K)\Delta t}|Y_0|^2, && k = 0 \\
S_{yy}(f_k) &= \frac{1}{(N+K)\Delta t}[|Y_k|^2 + |Y_{N+K-k}|^2], && k = 1, ..., \frac{N+K}{2} - 1 \\
S_{yy}(f_N) &= S_{yy}(f_{(N+K)/2-k}) = \frac{1}{(N+K)\Delta t}|Y_{(N+K)/2}|^2, && k = \frac{(N+K)}{2}
\end{aligned}
\tag{2.14}
$$

The signal variance σ_k^2 gives the total power of the spectrum through the summation

$$
\sum_{n=0}^{N+K-1} \sigma_k^2 = \sum_{n=0}^{N+K-1} S_{yy}(f)\Delta f \tag{2.15}
$$

When describing the wavenumber or frequency distribution in the spectra the colors red, blue and white from the electromagnetic spectrum can be used. Hence a red spectrum has a decreasing spectral level with increasing wavenumber, a blue spectrum has a increasing spectral level with increasing wavenumber and a white spectrum is flat with increasing wavenumber.

2.4 Fine Scale parameterization

Dissipation of internal wave energy and the diapycnal diffusivity for density are associated with small scale turbulence. For calculating the viscous dissipation of turbulent kinetic energy, ε, the horizontal velocity profiles can be used in the internal-wave parameterization presented by Gregg (1989). According to this parameterization $\varepsilon \propto E_{IW}^2$. The energy level of the internal wave field E_{IW} is a key ingredient in the parameterization and can be inferred by comparing the shear data with the GM estimate of shear variance. Observed shear can be obtained as fine-scale (10 m) first differencing of the velocity profiles. This, of course, does not account for the shear variances integrated to 10 m wavelength. The observed shear variance having wavelengths larger than 10 m is

$$
\langle V_{z_{10}}^2 \rangle = 2.11 \left[(\triangle u/\triangle z)^2 + (\triangle v/\triangle z)^2 \right] \qquad [\mathrm{s}^{-2}] \tag{2.16}
$$

where $\triangle z$= 10 m and the factor 2.11 is found to be the attenuation to account for 10 m sampling and first-differencing. The ratio of the observed internal wave energy to that of GM can then be obtained as

$$\frac{E_{IW}}{E_{GM}} = \frac{\langle V_{z_{10}}^2 \rangle}{\langle V_{z_{10}}^2 \rangle_{GM}} \tag{2.17}$$

where $\langle V_{z_{10}}^2 \rangle_{GM}$ is obtained from Eq. (2.11) using $\beta_u = 2\pi/$ 10 m. Using

$$\langle E_{IW}^2 \rangle = E_{GM}^2 \frac{\langle V_{z_{10}}^4 \rangle}{\langle V_{z_{10}}^4 \rangle_{GM}} \tag{2.18}$$

gives the internal-wave parameterization

$$\langle \varepsilon \rangle = \varepsilon_0 \langle \frac{N^2}{N_0^2} \rangle \langle \frac{\langle V_z^2 \rangle^2}{\langle V_z^2 \rangle_{GM}^2} \rangle \qquad \left[\mathrm{Wkg}^{-1}\right] \tag{2.19}$$

where ϵ is the average dissipation rate of kinetic energy due to internal waves, $\varepsilon_0 = 7 \times 10^{-10}$ W kg^{-1}, N is the buoyancy frequency and $N_0 = 5.2 \times 10^{-3}\mathrm{s}^{-1}$ is the reference buoyancy frequency. $\langle V_z^2 \rangle$ is the observed shear variance having wavelengths larger than $1/z$ m and $\langle V_z^2 \rangle_{GM}$ is the corresponding empirically derived shear in the Garrett and Munk spectrum of internal waves. Gregg (1989) uses XCP profiles and $z = 10$ m, hence $\langle V_z^2 \rangle_{GM} = 0.7N^2$ (Gregg & Kunze 1991) . The only variables are then N and $\langle V_z \rangle$ which are calculated by first differencing, and brackets indicate averaging.

Gregg (1989) parameterization uses only shear measurements. More recent improvements lead to parameterizations which also include strain (Gregg et al. 2003, Kunze et al. 2006)

$$\langle \varepsilon \rangle = \varepsilon_0 \langle \frac{N^2}{N_0^2} \rangle \frac{\langle V_z^2 \rangle^2}{\langle V_z^2 \rangle_{GM}^2} h\left(R_\omega\right) L\left(f, N\right) \tag{2.20}$$

Kunze et al. (2006) includes a correction in the latitudinal variation

$$L\left(f,N\right)=\frac{f\text{arccosh}\left(\frac{N}{f}\right)}{f_{30}\text{arccosh}\left(\frac{N_0}{f_{30}}\right)} \tag{2.21}$$

where f_{30} is the inertial frequency at 30° latitude, and for the variation in the shear-strain ratio R_ω

$$h\left(R_\omega\right)=\frac{3}{2\sqrt{2}}\frac{R_\omega+1}{R_\omega\sqrt{R_\omega-1}} \tag{2.22}$$

where $R_\omega=\frac{\langle V_z^2\rangle}{N^2\langle\xi_z^2\rangle}$. For the GM spectrum $R_\omega=3$. Using about 3500 hydrography/current profiles from the Indian, Pacific, North Atlantic and Southern Oceans, Kunze et al. (2006) obtain R_ω between 4-15 with a mean of $R_\omega=7\pm3$.

2.5 Inferring eddy diffusivity from dissipation

We can reach from the dissipation rate estimate to the diapycnal diffusivity using the Osborn (1980) model. Assuming steady-state, homogeneous turbulence and neglect the transport terms, the TKE budget equation is simplified to a balance between the shear production, buoyancy (B) and the dissipation rate of energy (ε).

$$-\overline{u'w'}\frac{\partial\bar{u}}{\partial z}+B=\varepsilon \tag{2.23}$$

The flux Richardson number (Ri_f) is the rate of energy loss by buoyancy to the rate of production of shear

$$Ri_f=\frac{-B}{-\overline{u'w'}\frac{\partial\bar{u}}{\partial z}} \tag{2.24}$$

Using $\overline{w'\rho'}=-K_\rho\frac{\partial\bar{\rho}}{\partial z}$, where K_ρ is the diapycnal eddy diffusivity, we get $B=-K_\rho N^2$.

This gives

$$K_\rho = \frac{R_f}{1 - R_f} \frac{\varepsilon}{N^2} = \gamma \frac{\varepsilon}{N^2} \tag{2.25}$$

where $\gamma = \frac{R_f}{1-R_f}$ is the mixing efficiency estimated to be 0.2 (Gregg et al. 1986) and ε is the dissipation rate. When fine scale shear profiles are available, together with a density profile, Eq. (2.19) can be used to obtain ε, leading to K_ρ through Eq. (2.25). The advantage of using Eq. (2.19) for ε in Eq. (2.25), is that V_z and N are much easier to measure than ε (D'Asaro & Morison 1992).

Using Eq. (2.25), the internal wave induced mixing parameterizations become

$$K_\rho = K_0 \langle \frac{\langle V_z^2 \rangle^2}{\langle V_z^2 \rangle_{GM}^2} \rangle \qquad \left[\mathrm{m^2 s^{-1}}\right] \tag{2.26}$$

for Gregg (1989) and

$$K_\rho = K_0 \frac{\langle V_z^2 \rangle^2}{\langle V_z^2 \rangle_{GM}^2} h\left(R_\omega\right) L\left(f, N\right) \tag{2.27}$$

for Gregg et al. (2003). Here $K_0 = 0.2 \varepsilon_0 N_0^{-2} = 5 \times 10^{-6}$ $\mathrm{m^2 s^{-1}}$.

2.6 Small scale processes in the Arctic

Breaking internal waves is an efficient way to mix the ocean interior, but is not the only mixing mechanism present in the Arctic Ocean. Padman (1995) gives a review of the small-scale physical processes in the Arctic Ocean, and a cartoon of the different mixing processes can be seen in figure (2.3). At the ocean boundaries this includes mixing due to e.g. friction at the seabed, surface stress at the air/sea or ice/sea interface and surface buoyancy fluxes produced by salt rejection during ice formation. Away from the ocean boundaries mixing can occur due to submesoscale eddies, internal wave instabilities (e.g. internal wave breaking) or double diffusion (i.e. diffusion of heat and salt where there is an increase in both with depth, diffusive convection, or a decrease in both with depth, salt-fingering). When the mixing is due to shear instabilities like breaking internal waves, the diffusivities for heat and salt are assumed to be equal, but when the mixing is due to diffusive convection the diffusivity for heat is greater than that for salt.

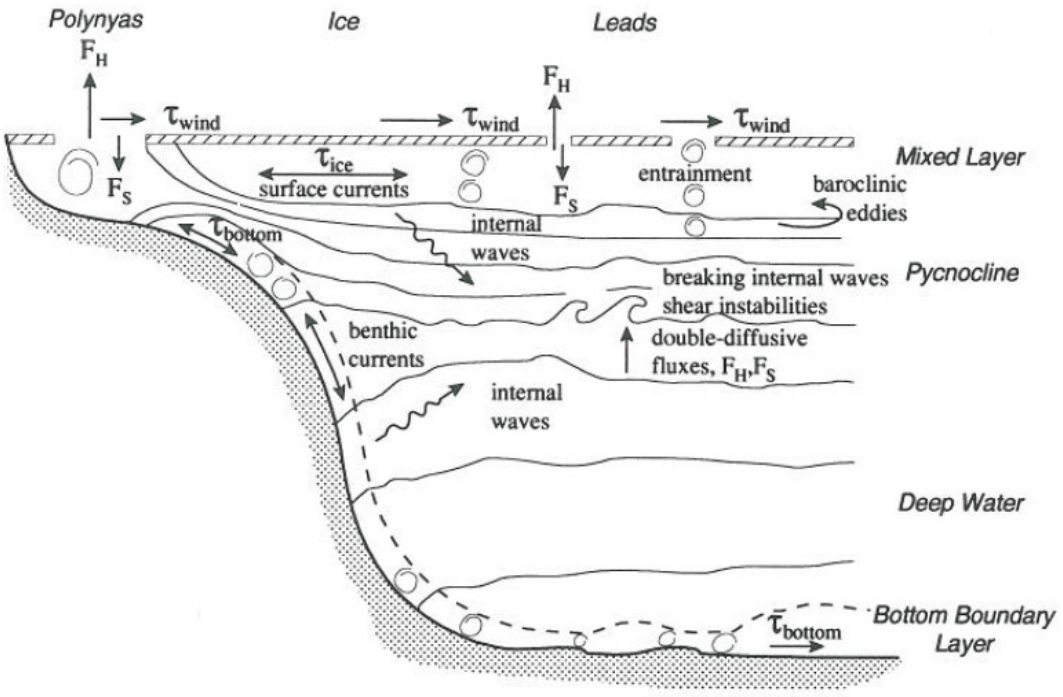

Figure 2.3: Mixing processes in the Arctic Ocean (Padman 1995) .

2.7 Relevant Past Work

2.7.1 Internal waves in the Arctic ocean

Measurements done in the Arctic show that internal wave energy levels are lower than what is observed at lower latitudes. The Arctic Ocean is hence also a region that deviates from the GM model. The parameters of the GM model can be combined into $r = E_{GM} b^2 N_0$ (Levine et al. 1985), where $r = 320$ m^2 cpm for the canonical GM field. The energy level r of the internal waves in the Arctic Ocean, determined from measurements, is compared with historical data from lower latitudes (figure (2.4)). Levine et al. (1985) use observations provided by a thermistor chain hanging from a drifting pack ice flow in May 1981. The observations were done over 5 days and measured oscillations in temperature, which is linked to vertical displacement of internal waves. The results shows a lower spectral energy in the Arctic Ocean compared with the GM model and the historical data.

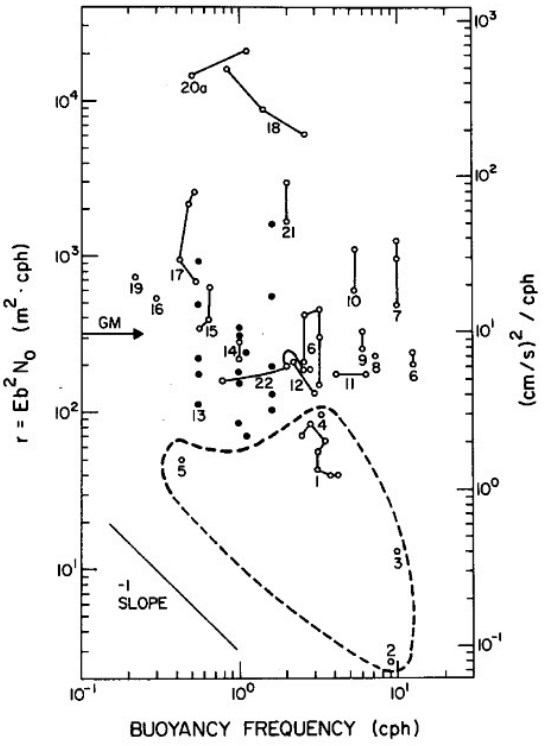

Figure 2.4: Estimates of the spectral level r, plotted against the local buoyancy frequency. The numbers refer to the historical data which are listed in Levine et al. (1985). The estimates from the Arctic Ocean are found inside the dashed line (Levine et al. 1985).

Using historical data Morison (1986) found the spectral levels of isotherm displacement to be about 0.05 to 0.33 times lower than the GM model and other internal wave observations at lower latitudes, but with a similar spectral shape. Possible explanations for the reduced energy level can be the ice cover as it eliminates most of the surface wave forcing. Morison et al. (1985) show, using a simple model of internal wave energy balance, that the predicted amount of dissipation can be great enough to explain the earlier observations of the low internal wave energies in the Arctic Ocean. Another contributing reason can be the lack of tides. In the Arctic the tides are weak and the dominant tidal frequencies lie outside the linear freely-propagating internal wave range above 75°N. Furthermore the presence of ice cover introduces a wall boundary layer where internal wave energy can be dissipated (Morison et al. 1985).

D'Asaro & Morison (1992) explored the internal wave shear levels in the eastern Arctic Ocean, using CTD and velocity profilers (mainly XCPs) deployed during MIZEX 83 and Polarstern Arktis IV/3. Shear levels were found to be consistently low over the abyssal plains, but comparable to the mid-latitude levels near rough topography in the Fram Strait. The finescale parameterization (Gregg 1989) resulted in diapycnal diffusivities that vary from about 10^{-6} to above 10^{-4} $\mathrm{m^2 s^{-1}}$. The XCP profiles deployed while drifting across a seamount on the Yermak Plateau, suggest an elevated shear level with $K_\rho \sim 10^{-4}$ $\mathrm{m^2 s^{-1}}$. It is further suggested that these higher shear levels can be explained by the internal wave generation by the barotropic tide on the seamount.

Fer et al. (2010) investigate the role of tides, internal waves and topography in mixing near the Yermak Plateau, using observations of oceanic currents, hydrography, and microstructure made in summer 2007. This data is less energetic compared with the elevated shear levels found over the seamount in D'Asaro & Morison (1992). Fer et al. (2010) suggest a large variability in the energy level over the plateau, and that the elevated shear may be a feature related to the seamount. Using the observed average shear-strain ratio together with the latitude dependence they obtain a revised estimate of the upper range diffusivity of about 6×10^{-5} $\mathrm{m^2 s^{-1}}$. It is suggested that these values are representative of the mixing in the Arctic over rough topography.

2.7.2 Near-inertial internal wave propagation in the Arctic Ocean

The temporal and spatial variability of the western Arctic internal wave field was investigated during the yearlong Surface Heat Budget of the Arctic (SHEBA) experiment

(Pinkel 2005). Through monitoring of the velocity and shear fields in the upper ocean by a Doppler sonar, near-inertial internal waves were found to be the dominant contributor to the super-inertial motion field (i.e. the internal wave continuum between f and N).

The near-inertial waves may contribute to deep mixing in the Arctic Ocean when they reach continental slopes and shelf areas. There are two scenarios on how inertial waves reach these areas (Pinkel 2005). First is trans-Arctic propagation where near-inertial waves propagate through the Arctic without much dissipation and contain energy for mixing when reaching land. The second is an one-bounce scenario where the local near-inertial internal wave generation contributes to deep mixing on nearby continental slopes. When these wave groups encounter the continental slope, they can forward reflect into shallow water, backreflect into the deep sea, or dissipate in a near-bottom boundary layer. What happens is determined by the slope of the seafloor (see section (2.1)). Much of the continental slope in the western Arctic is close to the critical angle for near-inertial wave reflection.

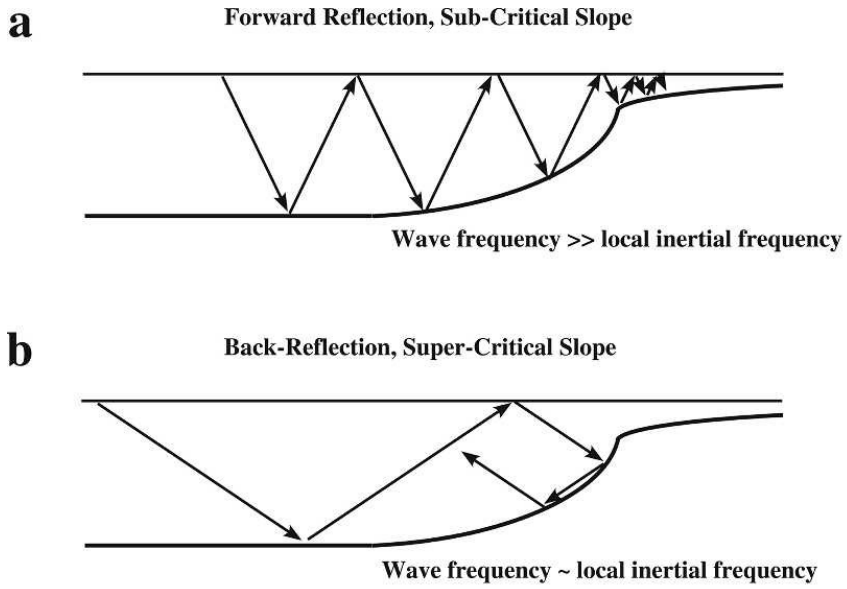

Figure 2.5: Two internal wave scenarios, a) forward reflection and b) back reflection (Pinkel 2005)

Pinkel (2005) finds the one-bounce scenario more consistent with the results than the trans-Arctic propagation. The typical stratification in the Artic Ocean and the low internal wave frequency leads to small propagation angles. Due to this only energy from atmospheric forcing within $300 - 500$ km from the shelves will contribute to deep mixing, according to the one-bounce scenario. Roughly 60% of the Arctic Ocean is within 300 km

from shelf areas.

2.7.3 The Cold Halocline Layer in the Central Arctic

The cold halocline layer (CHL) is a strongly stratified layer under the sea-ice below the mixed layer, with the change in density dominated by the increase in salinity (Aagaard et al. 1981, Rudels et al. 1996). The CHL observed in the Arctic Ocean is maintained by a weak vertical diffusion, but can be destroyed by an average eddy diffusivity of 5×10^{-5} m^2s^{-1} and larger. Currently the CHL prevents the Atlantic water from reaching the upper part of the ocean and the ice cover. Fer (2009) used early spring measurements of hydrography, shear and temperature microstructure to determine the diapycnal eddy diffusivity, the eddy diffusivity for heat and the turbulent flux of heat. These measurements were done during calm circumstances without any storm and eddy events in the upper water column, and covered the core of the Atlantic Water. The observations show an oceanic heat flux across the cold halocline that is not significantly different from zero. The eddy diffusivity levels in the upper cold halocline is low and show small vertical turbulent transport of heat, and the cold halocline is maintained.

2.7.4 Internal wave energy dissipation under sea ice

The internal wave energies under the sea ice in the Arctic Ocean may be low because of increased energy dissipation. The surface boundary layer dissipation process is unique to ice-covered regions, and the predicted amount of dissipation appears to be great enough to explain earlier observations that the internal wave energy in the Arctic Ocean is low compared to the internal wave energy measured in ice-free oceans. An illustration of the difference in dissipation between ice-covered ocean and an ice-free ocean is seen in figure (2.6).

Morison et al. (1985) use a time-varying boundary layer model with an eddy coefficient closure scheme, which is solved numerically, to investigate whether the internal wave energy may be less in ice covered waters because of increased surface boundary layer dissipation under the ice. The main goal of the model is to obtain a realistic estimate of the periodic boundary mixing, and therefore the nonlinear interactions of the waves in the boundary layer are ignored. It is assumed that the velocity scale and magnitude of the eddy coefficient are determined by the mean flow and are independent of the internal wave field. The boundary layer dissipation occurs only in the presence of an ice cover.

Morison et al. (1985) conclude that surface boundary layer turbulence is important in the dissipation of internal wave energy and may be a possible explanation of the reduced internal wave energy in the Arctic. It is also suggested that the under ice boundary topography may produce other changes in the internal wave spectrum of the Arctic (e.g. ice keels and other small-scale features can generate internal waves).

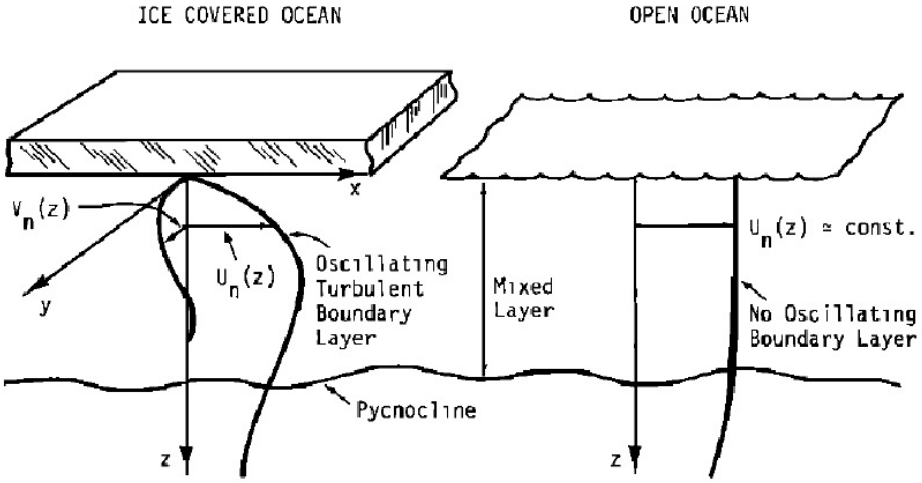

Figure 2.6: The difference in internal wave boundary conditions between an ice-covered ocean and an ice-free ocean, including the boundary layer coordinates (Morison et al. 1985).

2.7.5 Increase in near-inertial shear in the seasonally ice-free Arctic

The ice cover shelters the underlaying ocean from the wind and dampens the wind driven mixing. Internal waves and this wind-driven mixing can, however, become more important as the ice cover retreats. From moored measurements Rainville & Woodgate (2009) present seasonal observations under a varying sea-ice cover, of the internal wave level. The observations are made during a 2-year period on the continental shelf in the northern Chukchi Sea. The results show that the wind has no response on the ocean under the sea-ice. But during ice free periods local storms generate inertial oscillations and strong vertical shear (figure (2.7)). They imply that the recent retreat in the summer sea ice cover will lead to an increase in the internal wave generation over the shelf areas and maybe also over the deep waters, and conclude that during summer it is the wind-generated inertial waves that dominate the internal wave field. The increase in internal wave generation and enhanced mixing during the ice free times will have implications for

the CHL and oceanic heat flux.

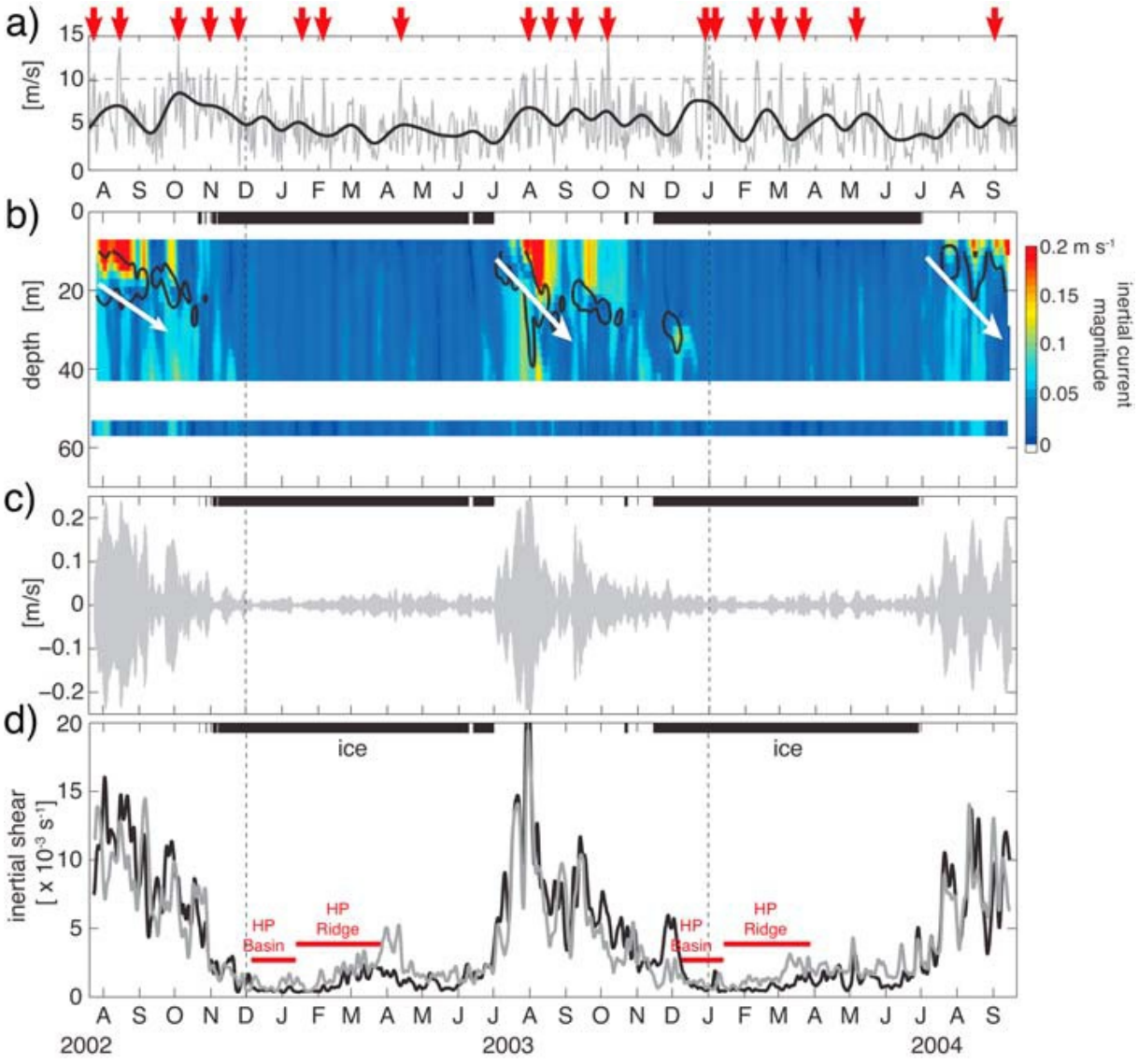

Figure 2.7: a) Daily (gray) and 30-day running-mean (black) wind speed at the mooring site. Red arrows indicate storms, defined as periods when daily wind speed exceeds 10 ms^{-1}, b) magnitude of the inertial currents as a function of depth and time in ms^{-1}. The white arrows indicate downward energy propagation c) time series of the east component of the inertial current at 10-m depth and d) smoothed time-series of inertial shear magnitude, between 10 and 30 m, black and grey lines indicates data from two different moorings. The red lines indicate mean shear results from a drifting ice camp. Thick black bars at the top of b), c) and d) indicate the presence of sea ice (Rainville & Woodgate 2009).

Chapter 3

Site, surveys and data

3.1 Site

The Arctic Ocean consists of two large basins, the Amerasian Basin and the Eurasian Basin, separated by the Lomonosov Ridge (figure (3.1)). The Nansen-Gakkel Ridge divides the Eurasian Basin into the Nansen and Amundsen basins. The Alpha-Mendeleyev Ridge divides the Amerasian Basin into the Canada and Makarov basins. Surrounding the basins are large shelf areas. The Arctic Ocean is connected to the Pacific Ocean through the Bering Strait, which is the source of Pacific Water, and to the Atlantic Ocean through the Fram Strait. Through the Fram Strait, warm and saline Atlantic Water enters the Arctic Ocean with the West Spitsbergen Current. Cold low-saline water leaves the Arctic Ocean with the East Greenland Current (Aagaard et al. 1985). Inside the Arctic Ocean two current systems dominate the surface circulation. The Transpolar Drift transports ice across the Arctic Ocean towards the Fram Strait. The Beaufort Gyre is a clockwise circulation located in the Beaufort Sea.

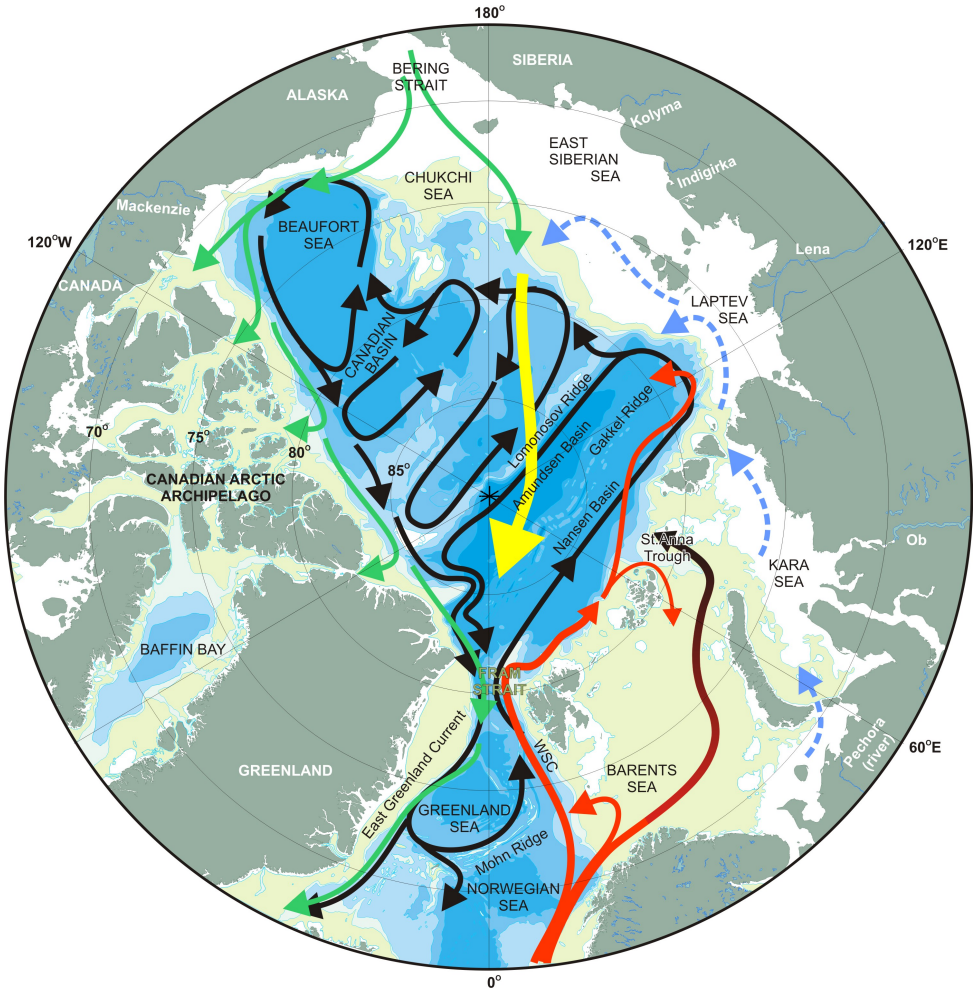

Figure 3.1: The bathymetry of the Arctic Ocean together with the path of the Pacific water (green arrows), the Atlantic Water (red arrow), the Transpolar Drift (yellow arrow), surface currents (blue dashed arrows) and the intermediate layer current (black arrows) (courtesy of Tor Gammelsrød).

3.2 eXpendable Current Profiler (XCP)

Velocity and temperature profiles were collected by XCPs. A short description of the XCP can be found in Sanford et al. (1993) and a more extensive description in Sanford et al. (1982). A specification sheet provided by the XCP manufacturer Lockheed Martin Sippican can be found at $http://www.sippican.com/stuff/contentmgr/files/5838b104aee77160ff44172515d2f214/sheet/xcp92005.pdf$. The principle of the XCP velocity measurements is electromagnetic induction by measuring the voltage generated as the seawater moves through the Earth's magnetic field relative to a depth independent mean. This is measured as the voltage difference between two electrodes. This provides relative hori-

zontal east (u) and north (v) velocity components. The XCP falls through the water with a speed of about 4 ms^{-1}, and is rotating at about 16 Hz. Measured velocity components are in error when the rotation frequency is smaller than 8 Hz. The depth is inferred from the time of the deployment and the known fall rate, which gives a vertical resolution of about 0.4 m.

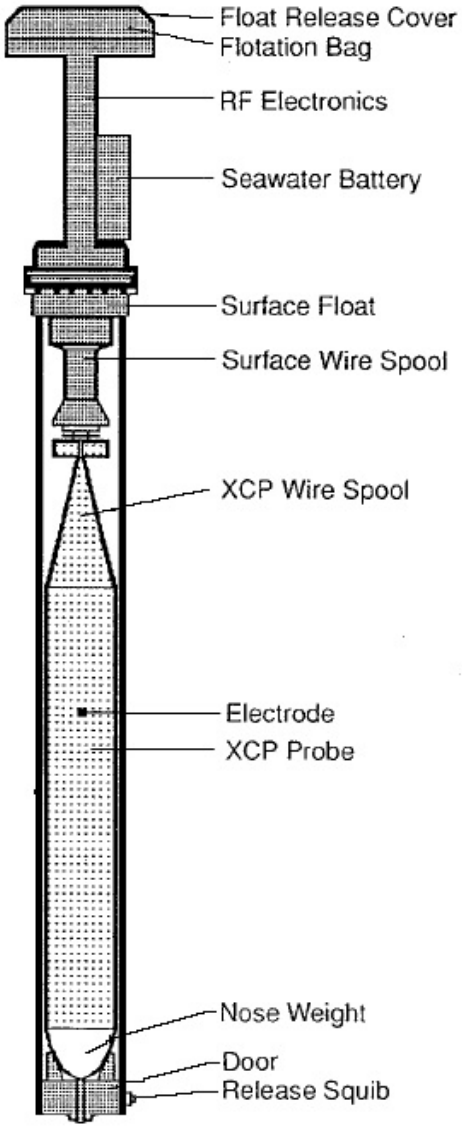

Figure 3.2: A simple illustration of the XCP probe. The probe is connected to a buoy at the surface through a wire ($\sim$ 1800 m on the latest XCPs) which transfers data. The probe contains electrodes and compass coil located at the center of the probe, and a thermistor mounted in the a hole in the center of the heavy noise weight (Sanford et al. 1993).

(a) (b) (c) (d)

Figure 3.3: Pictures showing a) a XCP recovered after the deployment, i.e. after the probe has been released from the buoy, b) the XCP transmitting data during a drop through a hole in the ice. The buoy and the antenna are seen, c) the set-up used in receiving and recording XCP data during the Borneo surveys. The small hand-held radio receiver which is connected to a digital sound recorder are seen and d) the experiment set-up during the drifting Borneo survey in 2008. The microstructure profiling is conducted in the tent and XCPs are deployed from a nearby hole. The receiver and sound recorder are seen in the case near the bottom of the picture (pictures by Ilker Fer).

The XCP probe is approximately 5 cm in diameter, 42 cm long and weighs about 900 g in seawater. The heavy nose of the probe makes it fall through the water. The probe contains electrodes for velocity measurements, a compass coil that determines the location of the magnetic north once per revolution, electronics, batteries, a thermistor to provide a vertical temperature profile and wire spooling components which transfer data to a small buoy with antenna at the surface. The XCPs can be launched from airplanes, ships in motion or deployed from a hole or opening in the sea-ice. An illustration of the XCP can be seen in figure (3.2) and pictures of the XCP and the experiment set-up can be seen in figure (3.3) .

The voltage measured by the electrodes are amplified and converted to a frequency modulated (FM) signal before transmitted to the buoy, and from the buoy the FM signals can be transmitted to a nearby location. For all the XCPs deployed in this study channel 14 is used which transmits data at 172.0 MHz. A description of the processing is found in section (3.5)

3.3 Microstructure profiler

A description of the microstructure profiler (MSS) can be found in Fer (2006). The MSS is a loosely-tethered free-fall instrument equipped with two airfoil probes aligned parallel to each other, a fast response conductivity and temperature probe, an acceleration sensor and conventional CTD sensors for precision measurements. As the instrument profiles vertically, the sensors point downward and they all sample at 1024 Hz.

The profiler is 1.4 m long, 106 mm in diameter and weighs ∼8 kg in air. The instrument is ballasted to free-fall at a typical fall speed of 0.6 - 0.7 ms^{-1} and is not influenced by operation induced tension as the cable is paid out at sufficient speed to keep it slack.

The MSS data are edited for transmission errors and spikes and then averaged to 256 Hz to reduce noise. Time series are converted into vertical wavenumber space using a smooth fall-speed profile and Taylor's frozen turbulence hypothesis. The fall speed is derived from the time derivative of the pressure record. The dissipation rate of turbulent kinetic energy per unit mass, ε, is calculated using the isotropic relation $\varepsilon = 7.5\nu\langle u_z^2\rangle$, where ν is the viscosity of seawater and u_z is the shear of the horizontal velocity resolved at cm-scales. Shear wavenumber spectra are calculated using 1 s segments and the shear variance which is obtained by integrating the shear wavenumber spectrum from 2 cpm to upto 30 cpm, depending on the shear variance. The eddy diffusivity is then approximated using the Osborn (1980) model (see section (2.5)).

3.4 Surveys

The dataset used consists of a total of 127 XCP casts deployed during various surveys between 1993 and 2010. Details of the deployments are tabulated in the Appendix, (table (1) to (10)). A map showing the locations of the XCP deployments from the different surveys is shown in figure (3.4). A brief description of the different data sets and processing of data is given in the following.

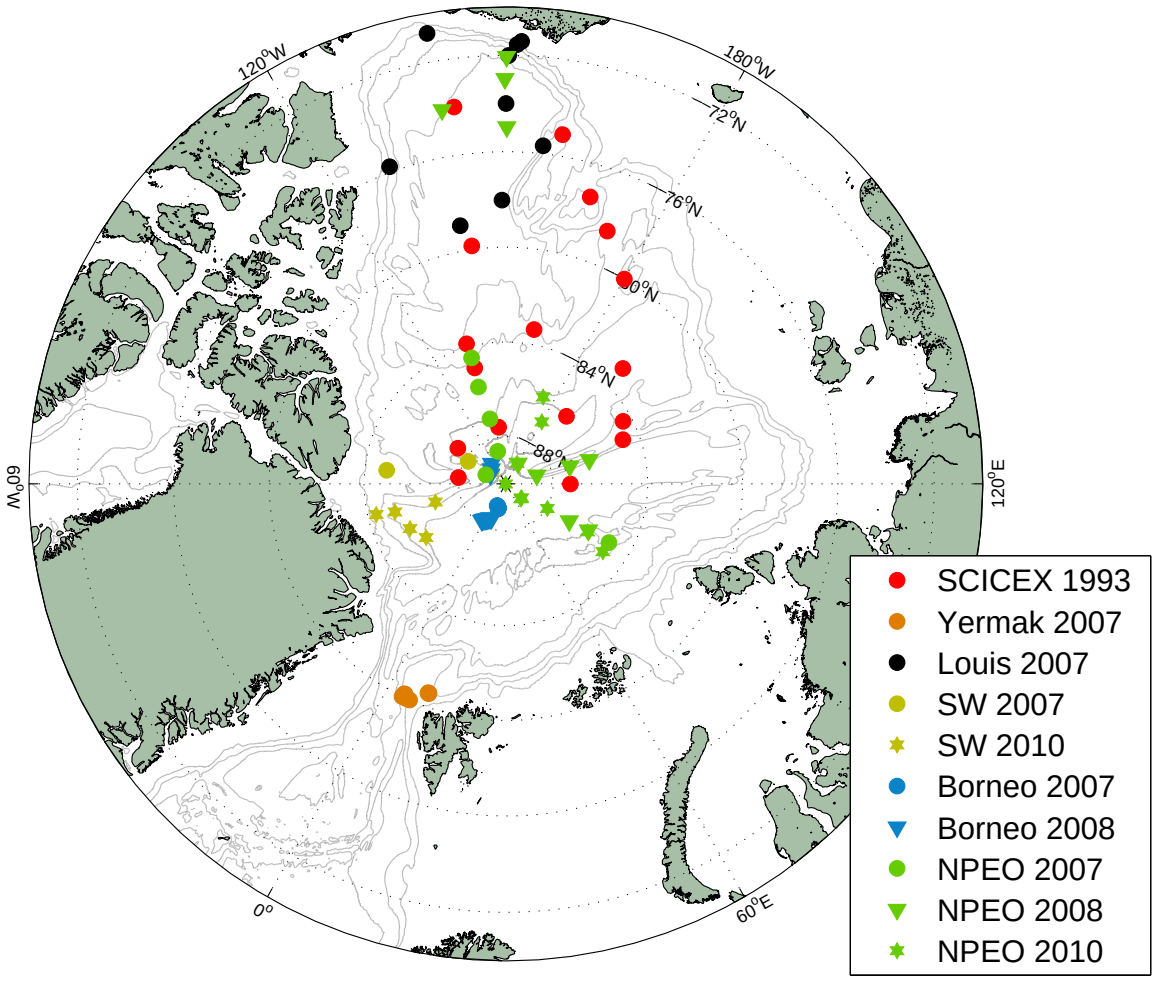

Figure 3.4: The location of the XCP deployments together with the bathymetry. Isobaths are drawn at 1000m intervals.

3.4.1 SCICEX 1993

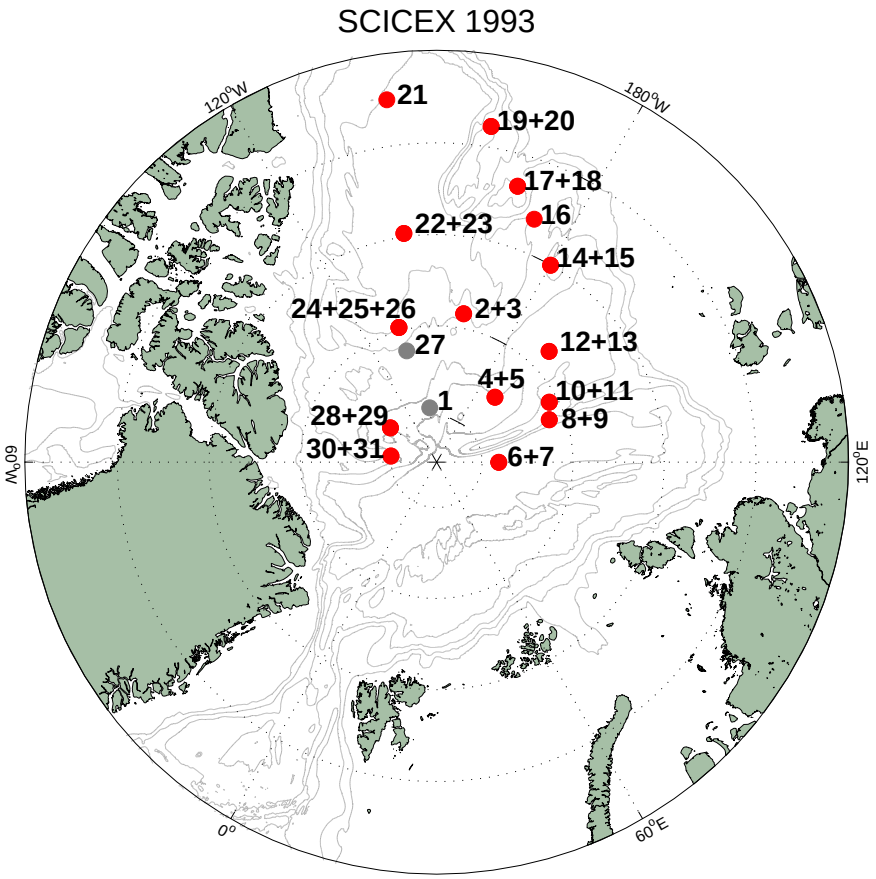

Figure 3.5: The location of the different XCP drops deployed during the SCICEX 1993, with the corresponding drop numbers. Drops 1, 2, 25, 27 and 31 returned no or bad data. Grey color indicates stations with no or bad data.

In August to September 1993, the scientific cruise with the nuclear submarine U.S.S. Pargo was the first civilian oceanographic submarine cruise in the Arctic Ocean (Morison et al. 1998). This was a part of the SCience ICe EXercise (SCICEX) program (referred to as SCICEX 1993 hereafter). During this cruise 31 XCP drops were made at 20 different surface CTD stations of the cruise. Drops 2, 27 and 31 failed and drop 25 returned bad data, and are not used in this analysis. Additionally, drop 1 has not enough CTD data to provide a buoyancy frequency profile. The location of the different XCP drops with corresponding drop number can be seen in figure (3.5). Density profiles from the surface CTD casts are used to calculate buoyancy frequency profiles, which are measured by a Sea-Bird SBE 19 probe.

3.4.2 North Pole Environmental Observatory

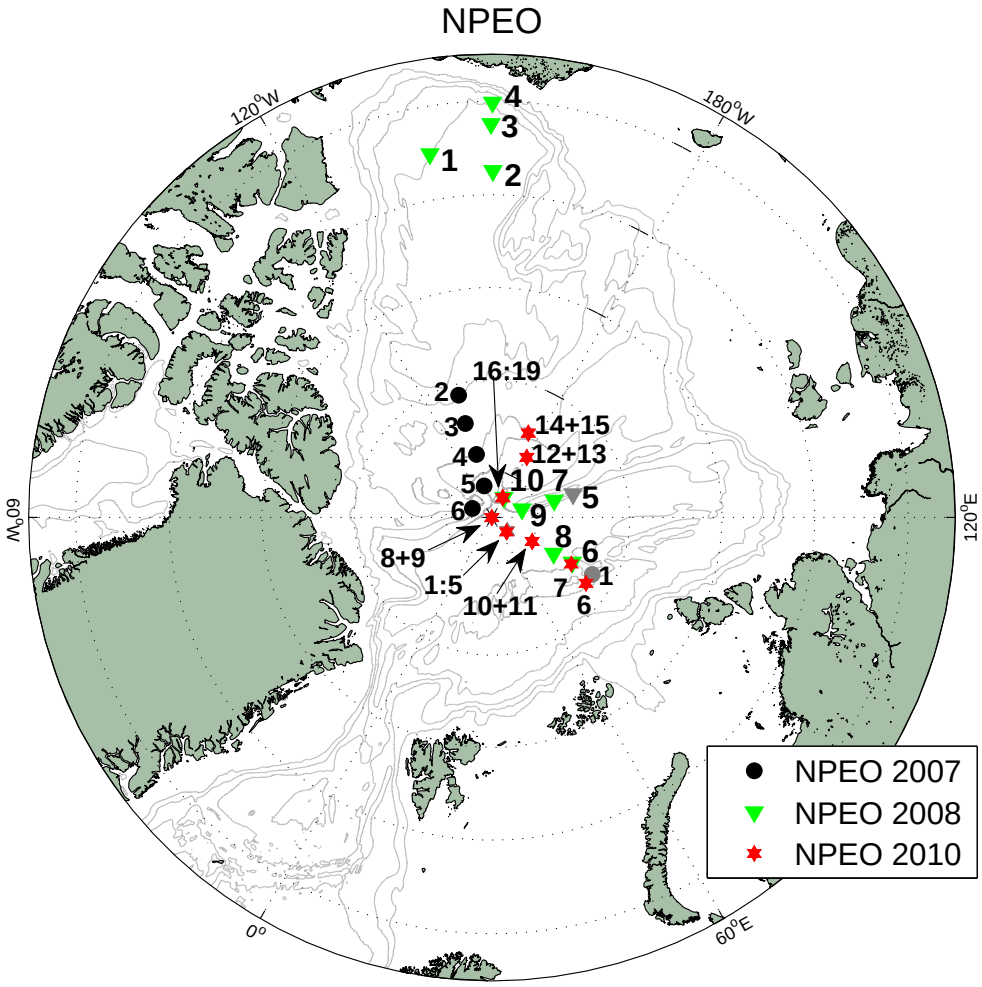

Figure 3.6: The location of the different XCP drops deployed during the NPEO 2007, NPEO 2008 and NPEO 2010, with the corresponding drop numbers. Grey color indicates stations where XCP drops returned no data or bad data. This concerns NPEO 2007 drop 1, NPEO 2008 drop 5 and NPEO 2010 drops 2,3,4 and 16.

Since 2000 the North Pole Environmental Observatory (NPEO) has done annual expeditions in April to the North Pole (*http* : *//psc.apl.washington.edu/northpole/*). The following XCP measurements were done at different positions on the Arctic sea ice after Twin Otter landings. During the 2007 survey (referred to as NPEO 2007 hereafter), 6 XCPs were deployed, where 5 returned data. During the International Polar Year (IPY), the aerial survey in 2008 was extended to the Beaufort Sea north of Alaska. During the

2008 survey (referred to as NPEO 2008 hereafter) 10 XCPs were deployed, which includes 4 in late March in the Beaufort Sea. Drop 5 failed. During the 2010 survey (referred to as NPEO 2010 hereafter) 19 XCPs were deployed. Drops 2 and 3 failed to record, and drops 4 and 16 returned bad data and are excluded from the analysis. Additionally density data from Seabird SBE-19plus Seacat CTD casts are used to calculate the buoyancy frequency profiles. The location of the different XCP drops with the corresponding drop number can be seen in figure (3.6).

3.4.3 Freshwater Switchyard

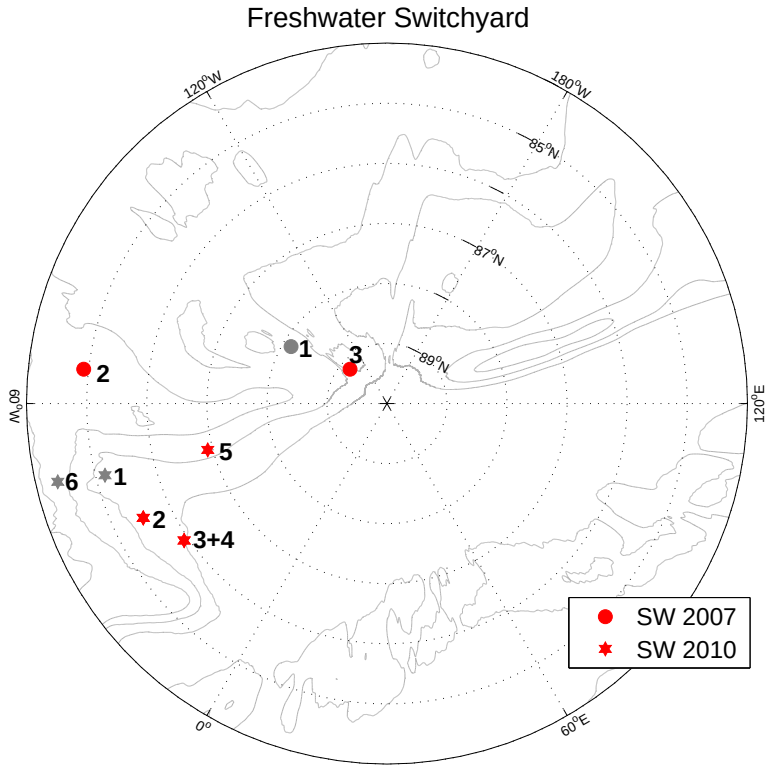

Figure 3.7: The location of the different XCP drops deployed during the SW 2007 and SW 2010, with the corresponding drop numbers. Grey color indicates where XCP drops returned no data or bad data. This concerns SW 2007 drop number 1 and SW 2010 drop 1,3 and 6.

The Freshwater Switchyard project (*http* : *//psc.apl.washington.edu/switchyard/index.html*) is partly a continuation, partly a spinoff, of NPEO. It investigates the variability of circulation, water mass properties and freshwater distribution in the area north of the Canadian

Archipelago and Greenland. In 2007 (referred to as SW 2007 hereafter), fog resulted in few data measurement, but 3 XCPs were deployed after Twin Otter airplane landings. Drop 1 failed. Twin Otter landings in 2010 (referred to as SW 2010 hereafter) resulted in 6 XCP deployments in the Lincoln Sea. Drop 6 failed and drops 1 and 3 returned bad data and are excluded from this analysis. Additionally density data from Seabird SBE-19 CTD casts are used to calculate the buoyancy frequency profiles. The location of the different XCP drops with the corresponding drop number can be seen in figure (3.7).

3.4.4 Louis 2007

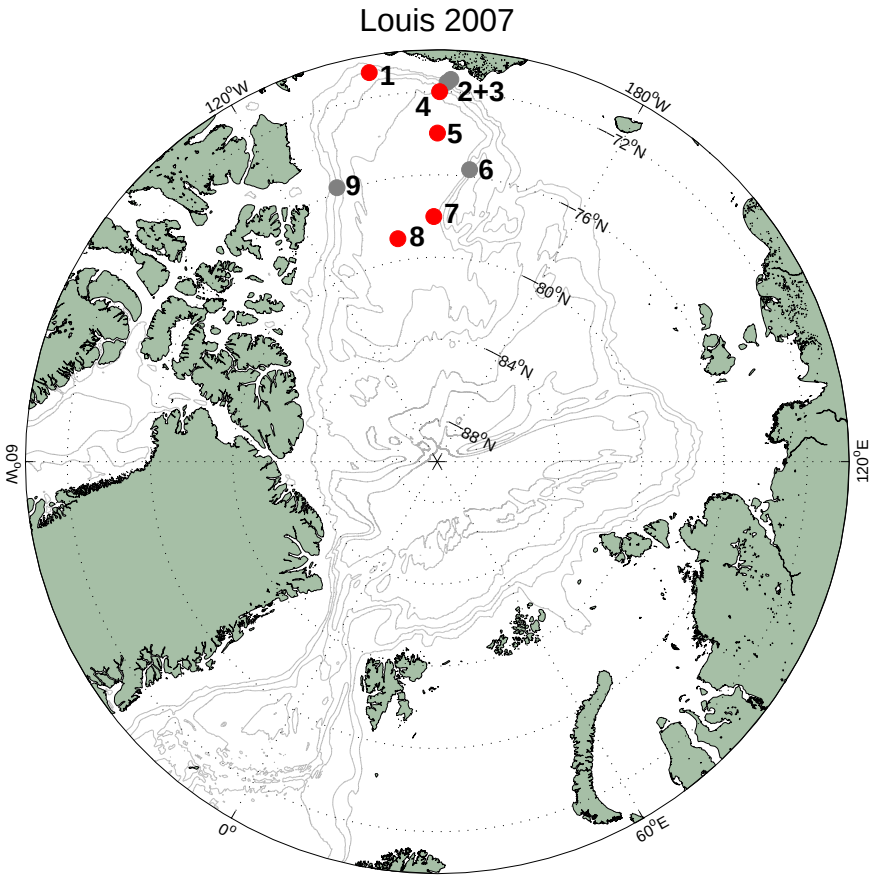

Figure 3.8: The location of the different XCP drops deployed during Louis 2007, with the corresponding drop numbers. Grey color indicates the stations where the XCP drops returned no or bad data (drops 2,3,6 and 9).

In August 2007 the Beaufort Gyre Exploration Project cruise with R.V. Louis St. Laurent took place in the Beaufort Sea. During this survey (referred to as Louis 2007

hereafter) 9 XCPs were deployed. Drops 2 and 9 failed and drops 3 and 6 returned bad data and are excluded from the analysis. The location of the different XCP drops with the corresponding drop number can be seen in figure (3.8). Additionally CTD casts from the Beaufort Gyre Project is used for the buoyancy frequency profiles estimates. This data set was collected and made available by the Beaufort Gyre Exploration Program based at the Woods Hole Oceanographic Institution (*http* : *//www.whoi.edu/beaufortgyre*) in collaboration with researchers from Fisheries and Oceans Canada at the Institute of Ocean Sciences.

3.4.5 Borneo

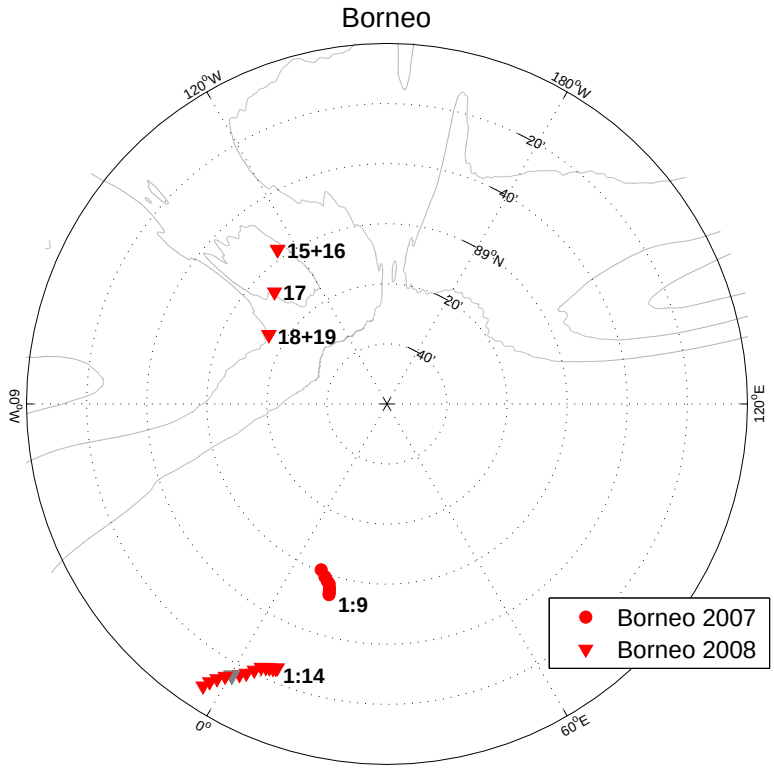

Figure 3.9: The location of the different XCP drops deployed during Borneo 2007 and Borneo 2008, with the corresponding drop numbers. Grey color indicates where XCP drops returned no or bad data. This concerns Borneo 2007 drops 1,2 and 7 and Borneo 2008 drop 10.

In 2007 and 2008, XCPs were deployed from the Russian ice base Borneo during its drift in the Amundsen Basin. In 2007 (referred to as Borneo 2007 hereafter) 7 XCP drops

were made, where drops 1,2 and 7 failed. In 2008 (referred to as Borneo 2008 hereafter) 19 XCP drops were made, with 5 XCPs deployed from three stations across the Lomonosov Ridge accessed by a helicopter. Drop 10 failed. The location of the different XCP drops with the corresponding drop number can be seen in figure (3.9). Additionally profiles of microstructure and hydrography were collected and the measured eddy diffusivity is used in comparison with the XCP derived eddy diffusivity.

3.4.6 Yermak 2007

In August 2007 observations were made of oceanic currents, hydrography and microstructurea during the cruise with R.V. Håkon Mosby near the Yermak Plateau (Fer et al. 2010) (referred to as Yermak 2007 hereafter). The site is where the marginal ice zone at the Arctic Front northwest of Svalbard is located. In this area warm Atlantic water is carried into the Arctic Ocean by the West Spitsbergen Current. 17 XPCs were deployed. Drops 3, 5, 7, 9 and 14 failed and drops 10 and 11 returned bad data and are excluded from this analysis. The location of the different XCP drops with the corresponding drop number can be seen in figure (3.10). Additionally microstructure and hydrography profiles were collected and the measured eddy diffusivity is used in comparison with the XCP derived eddy diffusivity.

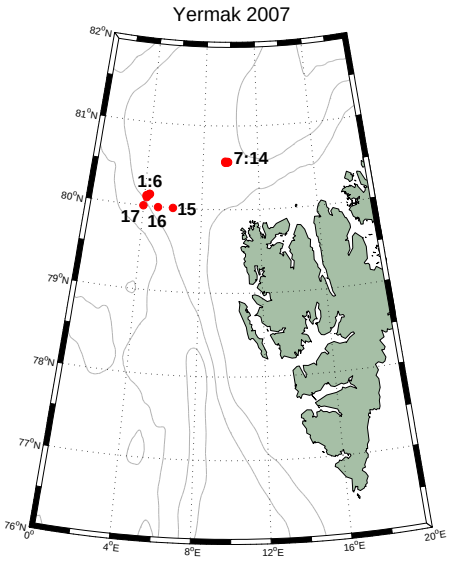

Figure 3.10: The location of the different XCP drops deployed during Yermak 2007, with the corresponding drop numbers. Grey color indicate where XCP drops returned no data or bad data. This concerns drops 3,5,7,9,10,11 and 14.

3.5 Data processing

The XCP manufacturer (Lockheed Martin Sippican) provides a commercial deck unit and software, Sippican MK21 system, for real-time data acquisition and processing, which can also be used for post processing by replaying sound files recorded at the field. Additionally, John Dunlap of the Applied Physics Laboratory, University of Washington, developed a MATLAB software (APL software hereafter), which is available at ($http://ohm.apl.washington.edu/\ dunlap/xcpdsp/$).

Both softwares require the horizontal intensity (F_h) and the negative vertical component (F_z) of the magnetic field. From the position and time of each XCP drop, horizontal intensity and the vertical component were obtained using the IGRF (11) model $http://www.ngdc.noaa.gov/geomagmodels/IGRFWMM.jsp$.

The details of the MK21 processing algorithms are not documented. Details of the APL software data processing can be found in Sanford et al. (1993). The start and end of a profile is detected by examining the record of rotation frequency to determine when the probe was released from the buoy at the surface and when it either reached the bottom or when the wire was torn. A time base is then constructed to infer the correct depths, from the known fall-rate, which can be assigned to the data. The sound signal converted into frequency, and together with the XCP probe rotation frequency, u, v and T profiles are produced as a function of depth. The data are then gridded at chosen vertical interval. The processing provides directly a plot of the rotation frequency, the temperature and its error, the u and v components of the relative velocity and the velocity error. An example from Borneo 2008 drop 8 can be seen in figure (3.11).

The processing of the APL software involves filtering and sinusoidal least-squares fitting to predefined segment lengths (chunk size) and velocity measurements are averaged in vertical bins (step size). The choice of chunk and step size has influence on the vertical wavenumber spectrum. After experimenting with different chunk and step sizes, it was decided to use 2 m chunks and 1 m steps, as this provided the most suitable spectral signature for fine-scale parameterization. Additionally after the APL processing, a Butterworth filter of order 7 is used to low-pass the velocity and temperature profiles with 4 m cutoff.

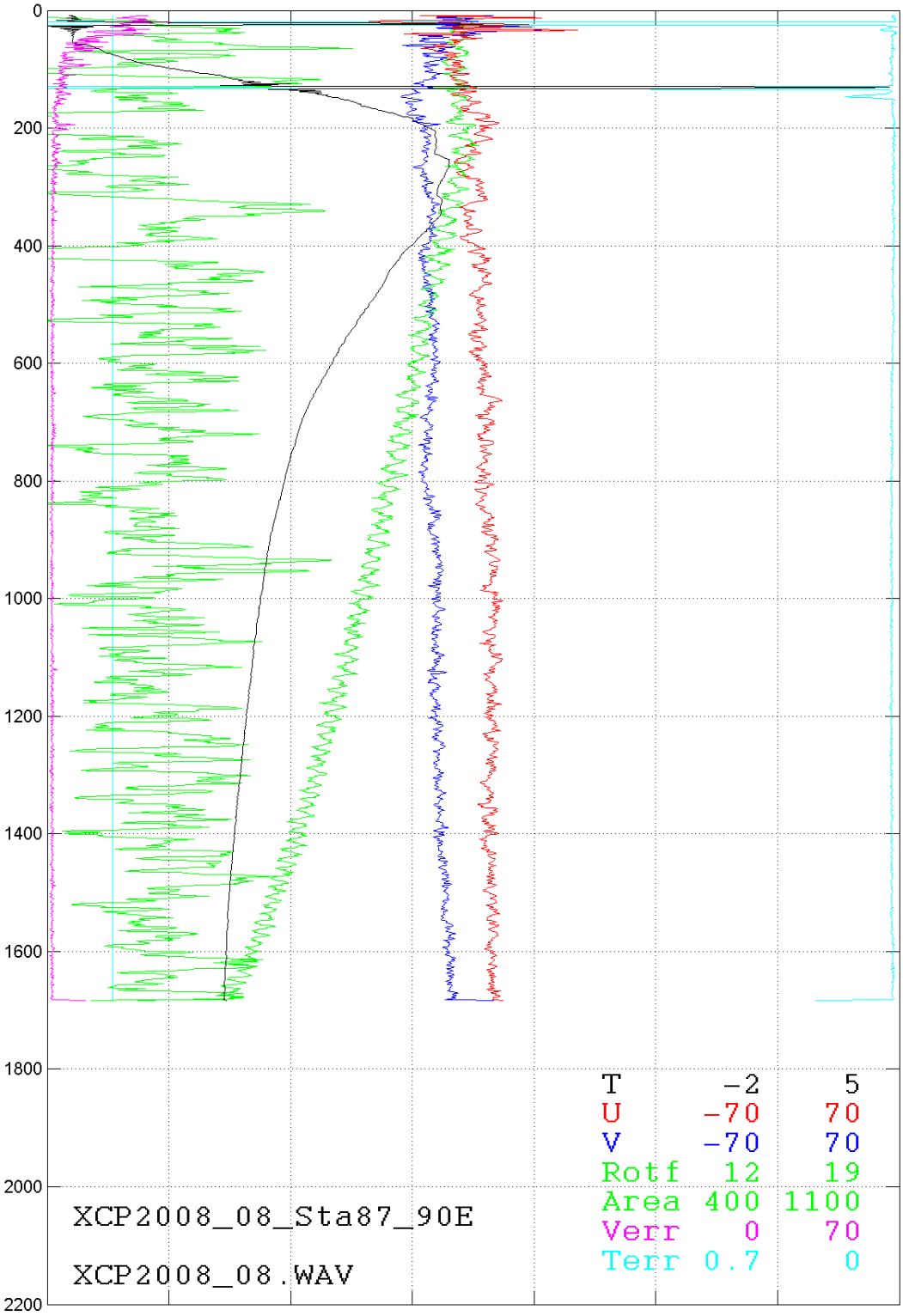

Figure 3.11: The APL processing plot from Borneo 2008 drop 8 using the soundfile XCP2008_08.WAV to get the processed textfile data saved as XCP2008_08_Sta87_90E. This shows the rotation frequency in Hz, the temperature and its error in °C, the u and v velocity in cms^{-1} and the v velocity error.

In figures (3.12) to (3.16), different chunk and step sizes are used to illustrate the difference when processing the data. The chunk and step sizes tested are listed in table 3.1. Profiles from two XCP drops are used to demonstrate the influence on the choice of processing; drop 8 from Louis 2007 and drop 9 from NPEO 2010.

Table 3.1: Different chunks and steps used in testing the processing routine.

Chunk size (m)	Step size (m)	Label
1	0.5	105
1	1	11
2	1	21
5	2	52

The relatively energetic upper 0-400 m and calmer lower 400-1400 m depth range is used from Louis 2007 and NPEO 2010, respectively, for calculating the spectra. The vertical profiles of velocity in u and v direction used in the corresponding energy spectra (figures (3.13) to (3.14)) are seen in figure (3.12), with the portion of velocity data used marked with a rectangle.

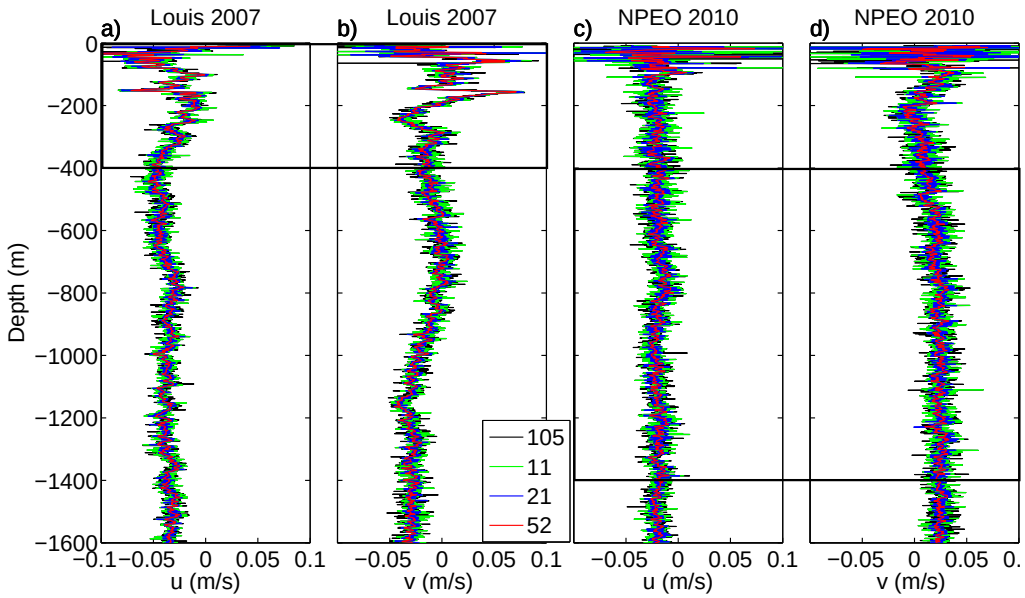

Figure 3.12: Profiles of a) u and b) v velocities for Louis 2007 drop 8 and c) u and d) v velocities for NPEO drop 9 after processed with different chunks and steps. Legends corresponds to the chunk and step sizes described in table (3.1) Depth ranges used for calculating the spectra in figures (3.13) and (3.14) are marked with rectangles.

This shows that increasing the chunk and step size clearly leads to smoother profiles in expense of the high wavenumber part of the spectra (figure (3.13)), which should be resolved to at least 1/10 m wavelength to apply the finescale parameterization. It also shows that chunk length 5 m significantly attenuates the high wavenumber portion near 0.1 cpm, whereas chunk lengths of 1 and 2 m give a good quality spectra. Profiles processed with 1 and 2 m chunk lengths are further smoothed using a low-pass Butterworth filter with 4 m cutoff. The influence of the low-pass filtering on the spectra is seen in figure (3.13c-d). While retaining the spectral properties to 0.1 cpm, the filtering leads to profiles with less noise.

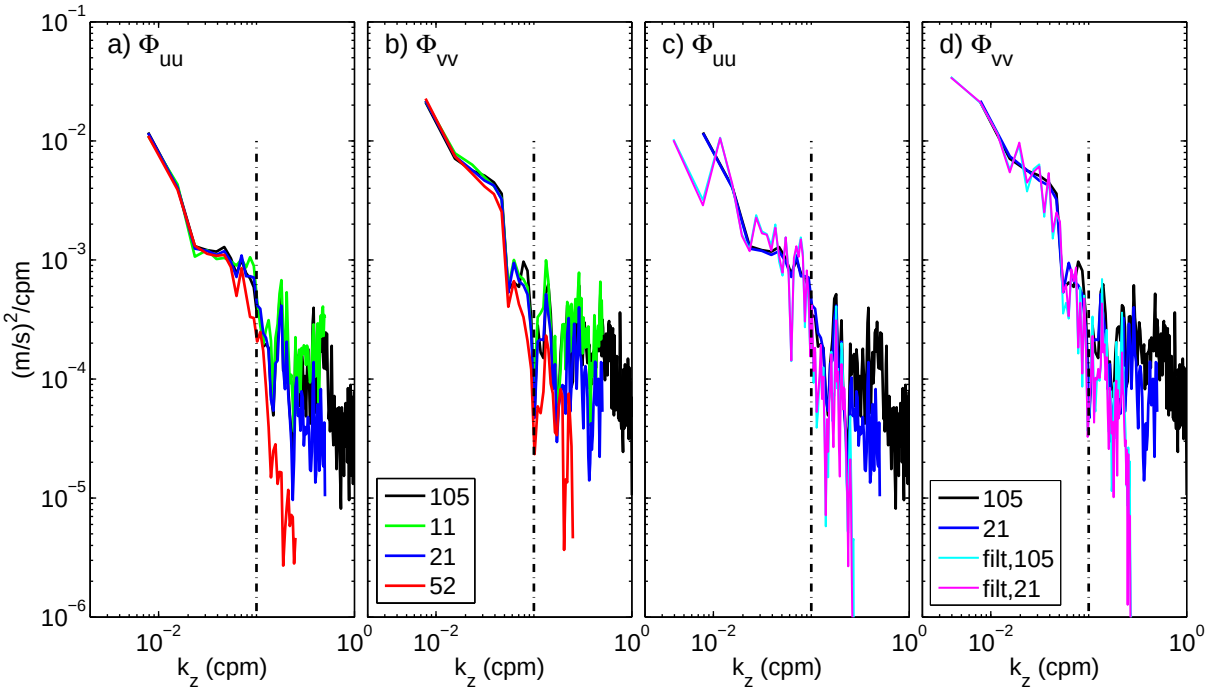

Figure 3.13: Upper a) u and b) v energy spectra from Louis 2007 drop 8. Legends correspond to the different chunk and step sizes used. Panels c) and d) show the difference in the u and v energy spectra, respectively, when using 1 m chunk and 0.5 m step and 2 m chunk and 1 m step and a Butterworth filter of order 7 and a 4 m cutoff (see legend). Vertical dash-dotted lines mark 0.1 cpm.

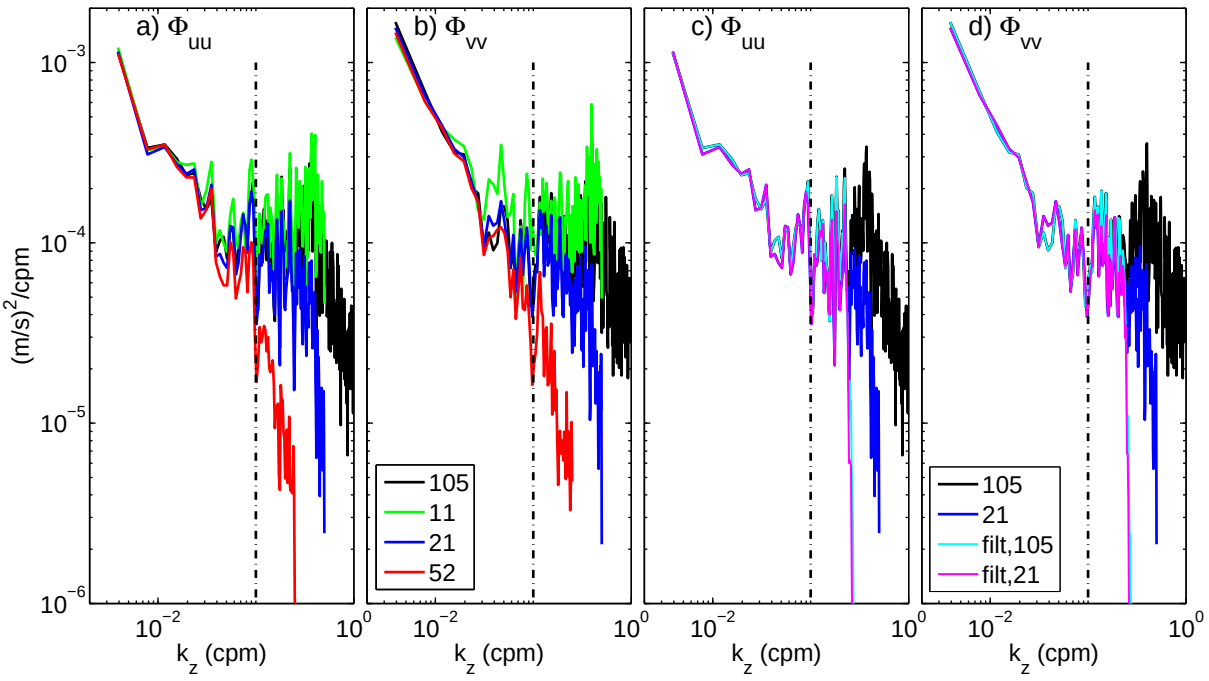

Figure 3.14: Same as figure (3.13), but for NPEO 2010 drop 9.

Furthermore, profiles of signal-to-noise ratio (SNR), defined as the ratio of velocity magnitude to the velocity error provided by the processing software, show that noise is greatly reduced for 5 m chunk length (figure (3.15)). However, sufficiently large SNR ($>> 1$) are also obtained for the 2 m chunk length, which does not corrupt the vertical wavenumber spectra at scales of interest. The total velocity spectra in figure (3.16), comparing the spectra of 2 m and 1 m chunks, do not show discernible difference, but the signal to noise ratio (figure (3.15)) gives better results using 2 m chunks and 1 m steps. We conclude that 2 m chunks and 1 m steps give the most convenient profiles for fine scale parameterization.

The drops used to illustrate the difference in processing were chosen because drop 8 from Louis 2007 and drop 9 from NPEO 2010 show, respectively, high and low signal to noise ratio. Figure (3.16) shows the difference in the energy level between the two drops, with Louis 2007 energy level being larger. The NPEO 2010 drop also gives a white slope after $k_z \sim 3\times10^{-2}$ cpm. This indicates noise, and the energy level at vertical length smaller than $\sim$ 33 m is higher than that would be obtained from a red slope. This should be noted for later sections as all profiles, regardless of their noise level, are first-differenced at 10-m scale and hence will result in unrealistic high eddy diffusivity.

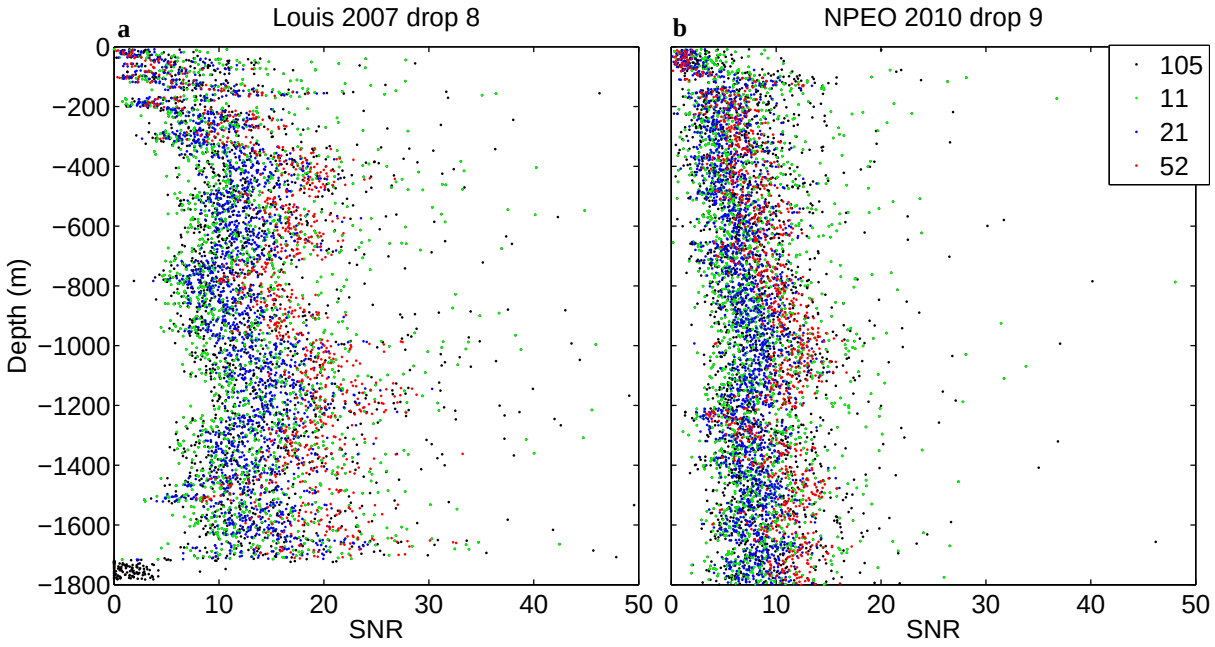

Figure 3.15: Profiles of signal to noise ratio after processing with different chunk and step sizes for a) Louis 2007 drop 8 and b) NPEO 2010 drop 9.

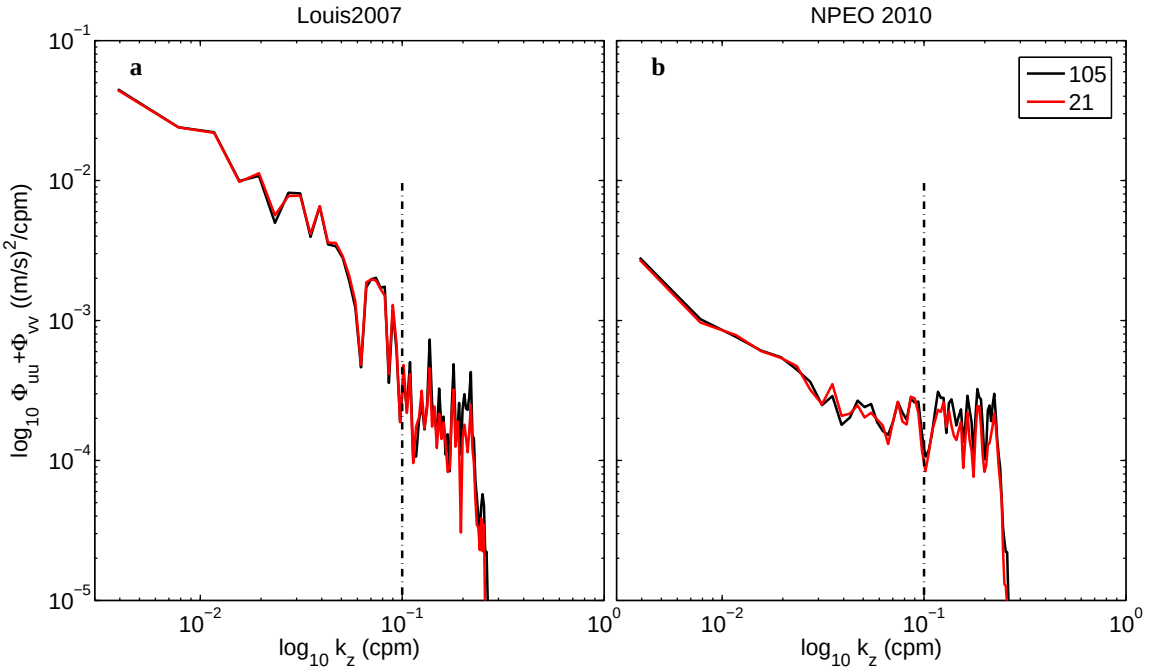

Figure 3.16: The total filtered velocity spectra for a) Louis 2007 drop 8 and b) NPEO 2010 drop 9 using 1 m chunk and 0.5 m step, and 2 m chunk and 1 m step. Vertical dash-dotted lines mark 0.1 cpm.

3.6 Comparison of MK21 and APL processing routines

The XCP data were initially processed using both softwares, however profiles and the spectral shapes differed significantly. The NPEO data set from 2010 was first processed with the Sippican MK21 software, and then the results were compared with the data processed with the APL software. As an example drop 9 from NPEO 2010 is presented, which has a low signal to noise ratio.

Vertical profiles of the u and v components of velocity can be seen in figure (3.17). The MK21 software gives many erroneous data points with the present set up, as it retains some data where the APL software excludes. The upper 400 m velocities are used to calculate the velocity variance spectrum shown in figure (3.18). From figure (3.18) it can be seen that the Sippican MK21 software processing gives a red slope, comparable to that expected from internal waves, which is an artifact of processing and hence not real. This red slope also resembles the result after processing with 5 m chunk and 2 m step in the previous section. Because the most important scale to resolve is about 10 m for internal wave and mixing studies (Gregg 1989), this spectral signature of the MK21 processing is not acceptable. In the following analysis all XCP profiles are obtained using the APL software.

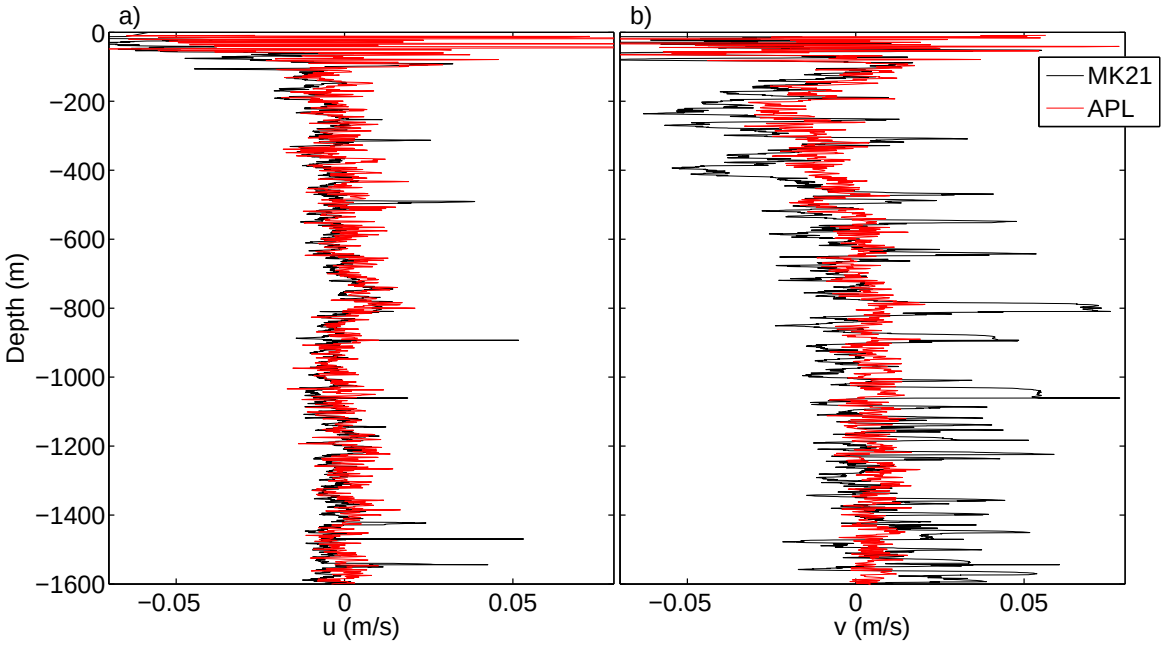

Figure 3.17: Profiles of u and v component of velocities (drop 9, NPEO 2010) after processing with MK21 and APL sofwares.

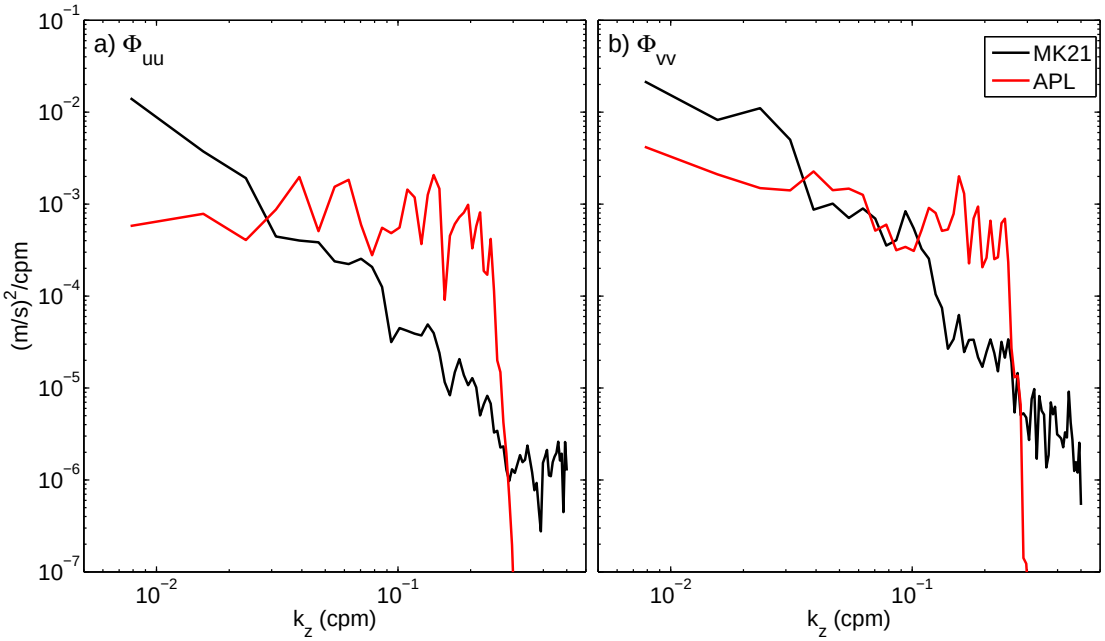

Figure 3.18: Vertical wavenumber spectra for a) u and b) v components after processing with MK21 and APL softwares.

3.7 Estimating K_ρ from XCP

After processing, the data were further edited before the profiles of K_ρ were calculated using the Gregg (1989) parameterization and the Osborn (1980) model (see section (2.4) and (2.5)). First large spikes in the velocity data were removed when there was a corresponding large velocity error. The XCP depth profile was corrected by comparing the XCP measured temperature profile with that provided by the CTD or MSS. While the XCP samples as deep as 1800 m, CTD profiles typically extend to about 500 m. Therefore the buoyancy frequency profiles needed for the eddy diffusivity calculations in the deeper part of the water column must be estimated. This was done by assigning the mean value in the deepest 50 m of the buoyancy frequency profiles to the deeper part of the XCP profiles. CTD measurements of only a couple of hundred meters will result in buoyancy frequency profiles of too large values in the deeper part and lead to erroneous eddy diffusivity data.

Following D'Asaro & Morison (1992) the XCP data were only retained if the corresponding CTD data provided the buoyancy frequency and if the XCP and CTD profiles of temperature agreed. The shear and its standard error ($\sigma_{V^2_{z_{10}}}$) were calculated from the slope of least squares line-fit of 10 m length scales (i.e. 10 data points) of the u and v velocity components against the depth. The standard error for shear is obtained from the misfit in the least squares sense. The data where $\sigma_{V^2_{z_{10}}}/N^2 > 1$ or $\sigma_{V^2_{z_{10}}}/V^2_{z_{10}} > 1$ were discarded as $\sigma_{V^2_{z_{10}}}$ is almost constant with depth, and N^2 and $V^2_{z_{10}}$ should be larger than the error.

The buoyancy frequency profiles can lead to incorrect values when measuring the vertical density gradient, as it can not be distinguished from zero for small values. The Osborn (1980) model is valid for stratified turbulence, and $K_\rho \propto N^{-2}$, which leads to unrealistically large eddy diffusivity if N is small. To avoid errors in the XCP profiles associated with weak stratification, the portions of the profiles with N less than 0.6 cph were discarded. The shear data were then used following directly the Gregg (1989) parameterization to infer the internal wave energy, and the Osborn (1980) model to infer the eddy diffusivity K_ρ.

Chapter 4

Results

4.1 Comparison with microstructure measurements

From Yermak 2007, Borneo 2007 and Borneo 2008, the microstructure profiles made it possible to compare the XCP derived eddy diffusivity with that inferred from the observed MSS profiles. Examples of one individual XCP drop from each survey, compared with the corresponding microstructure profile are seen in figure (4.1). These profiles are representative of each survey. An exception is drop 10 from Borneo 2008, see figure (4.2), where the XCP derived eddy diffusivity is about one order of magnitude larger than the microstructure profile. The XCP velocity data from this deployment, together with the drops before and after are shown in figure (4.3). The north component of the velocity profile from drop 10 differs from the ones done after and before, with the fluctuations being larger. This explains the high diffusivity inferred from this drop. This drop is clearly in error, however, survived the data screening.

The averaged diffusivity profiles from each of the three surveys are seen in figure (4.4), where the average is done over 10 data points and the vertical resolution is 5 m. Drop 10 from Borneo 2008 is not included in this average. The observed average microstructure diffusivity and the XCP derived diffusivity profile agree reasonably well. The noise level for the dissipation rate of turbulent kinetic energy measured by the MSS shear probe is 5×10^{-10} Wkg^{-1}. This is used in the Osborn (1980) model together with the buoyancy frequency profile from each cast to infer the noise (lowest detection) limit for the eddy diffusivity. The corresponding noise level in the averaged diffusivity profiles in figure (4.4) are shown as thin red lines. For the individual MSS profiles, all eddy diffusivity values below the noise level are removed.

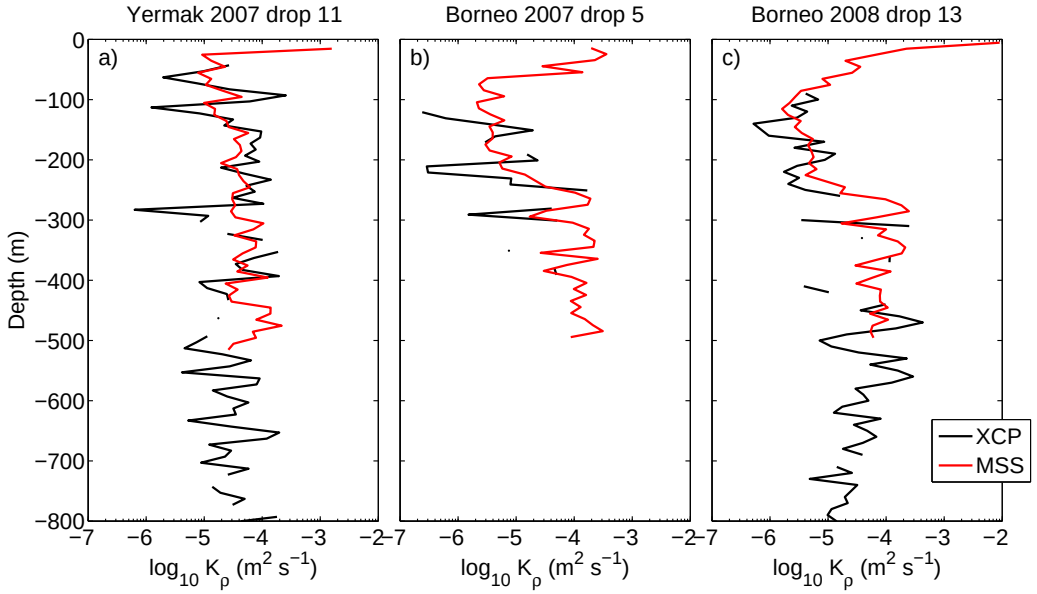

Figure 4.1: Individual profiles of 10-m averaged eddy diffusivity, K_ρ, inferred from the XCP deployment (black line) and the corresponding microstructure profile (red line) from each survey. a) Drop 11 from Yermak 2007, b) drop 5 from Borneo 2007 and c) drop 13 from Borneo 2008. The observed microstructure eddy diffusivity gives a smoother profile.

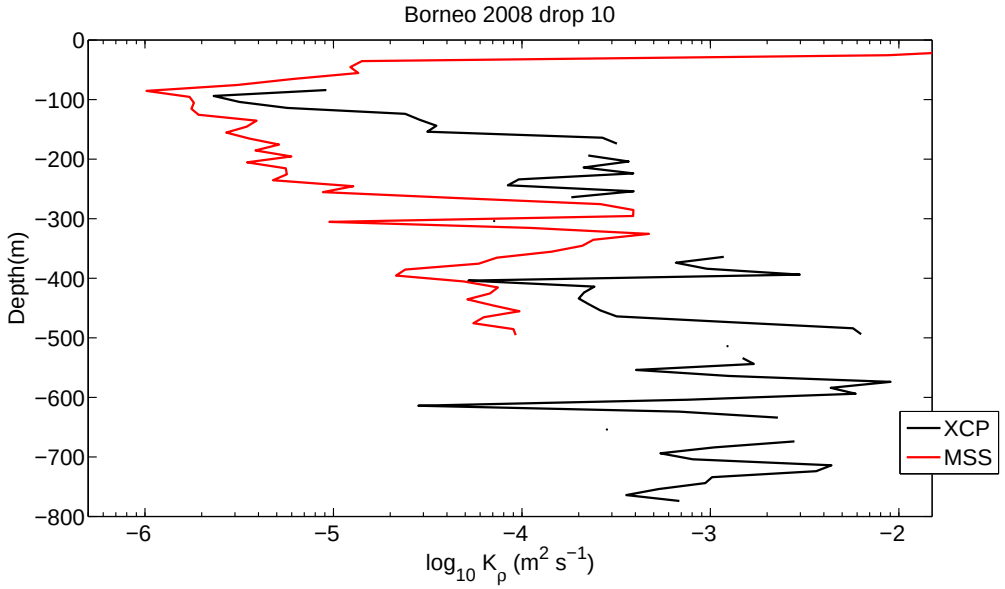

Figure 4.2: Eddy diffusivity profiles from Borneo 2008, drop 10 averaged at 10 m vertical resolution. The XCP derived eddy diffusivity is higher than the MSS.

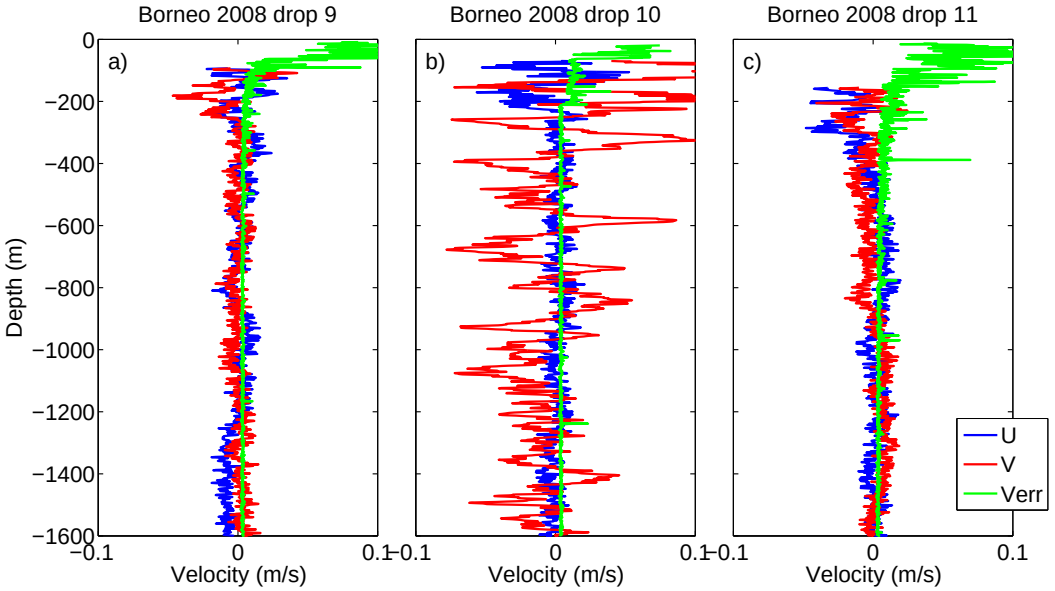

Figure 4.3: Velocity in u and v direction and the velocity error from Borneo 2008. a) drop 9, b) drop 10 and c) drop 11.

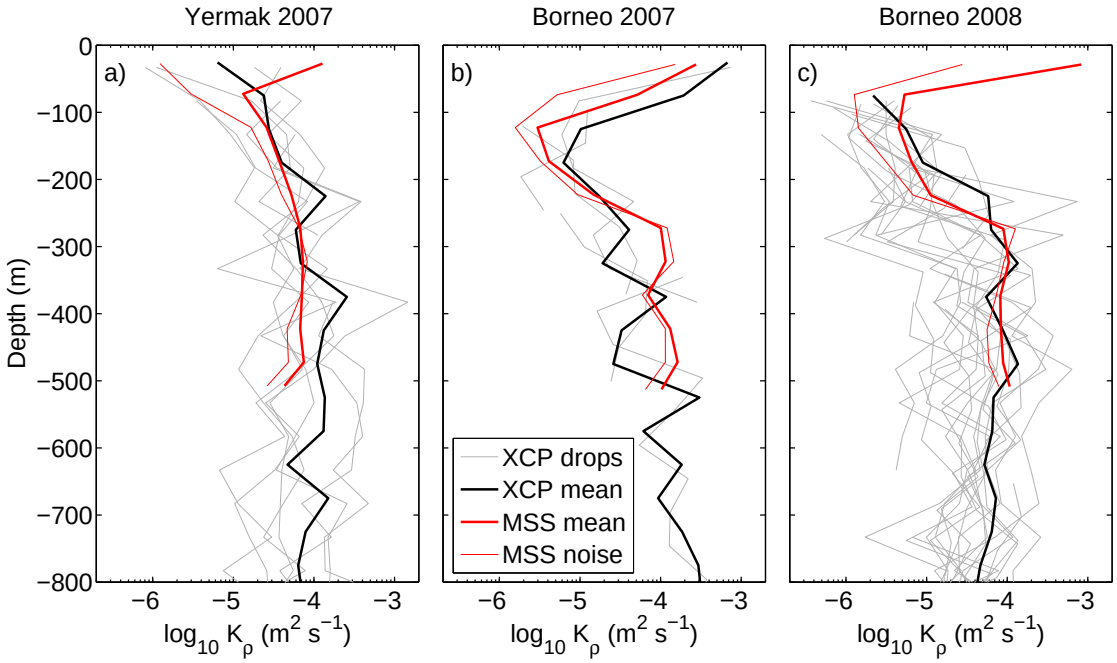

Figure 4.4: Averaged eddy diffusivity profiles from the different surveys. Grey lines are the individual XCP drops, black line is the average diffusivity from the XCP drops, thick red line is the average diffusivity from the microstructure profiles done at the same location and similar in time and the thin red line is the noise level for MSS diffusivity. Drop 10 from Borneo 2008 is not used.

Gregg (1989) parameterization does not account for the change in latitude and shear-strain ratio (section 2.4). We also test the revised parameterization Kunze et al. (2006) which includes correction terms for this variability. Figure (4.5) shows average survey profiles of eddy diffusivity derived from the XCP data using Gregg (1989), Kunze et al. (2006) and the MSS data. For Kunze et al. (2006) the correction in $h(R_\omega)$ is set to 0.37 corresponding to $R_\omega = 11$, which was derived from the Yermak survey in Fer et al. (2010). This is also imposed for the Borneo surveys, but R_ω is also allowed to range from 7 to 15, which gives an upper and lower error limit estimate for the Kunze et al. (2006) derived eddy diffusivity. For the rest of this chapter, the eddy diffusivity with a correction in $L\,(f, N)$ and $h(R_\omega) = 0.37$ is used.

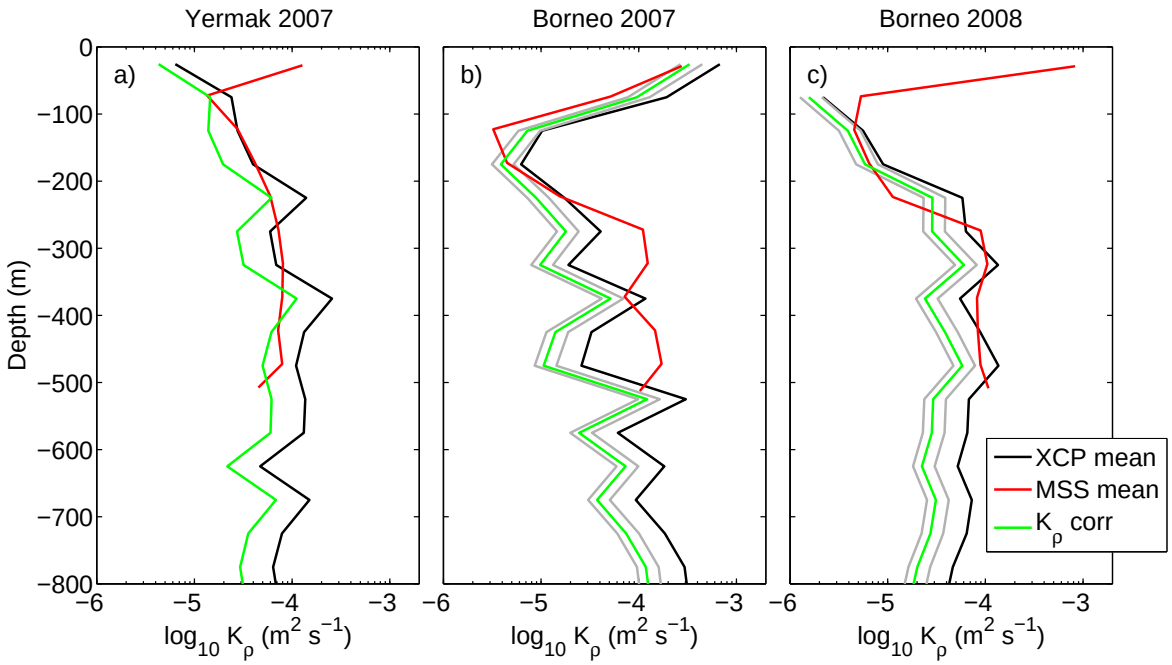

Figure 4.5: Averaged eddy diffusivity profiles from the XCP (black line) using Gregg (1989) parameterization, the direct measurements obtained from the MSS after removing values close to the noise level (red line) and the XCP where shear-strain ratio and latitude dependence is included in the internal wave parameterization (green line) using Kunze et al. (2006) and R_ω=11 . Grey lines indicate the upper and lower limits of Kunze et al. (2006), where R_ω is allowed to vary from 7 to 15.

The skill of the finescale parameterization is further presented by plotting XCP-derived and MSS-derived eddy diffusivity against each other (figure (4.6)). If the agreement was excellent the data points would all lay on the 1:1 line, but the result shows significant scatter. Note that turbulence is an intermittent phenomenon and profiles collected in the identical circumstances can show considerable scatter. Averaging can reduce this

variability. The data are therefore further averaged into equally-spaced logarithmic bins. The errorbars give the upper and lower 95% confidence limits on the maximum likelihood estimator expected from a logarithmic distribution (Baker & Gibson 1987).

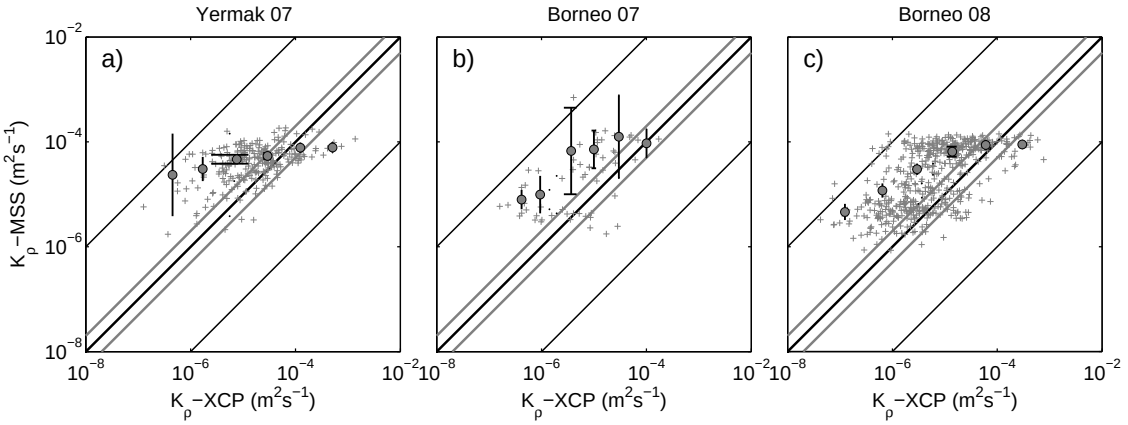

Figure 4.6: Averaged eddy diffusivity from the MSS and XCP measurements for a) Yermak 2007, b) Borneo 2007 and c) Borneo 2008. Diagonal lines envelope a factor of 2 and 100. Crosses are all the XCP data plottet against the corresponding MSS data. Bullets and the errorbars are the maximum likelihood estimator and the 95% confidence limits over log10-K_ρ bins.

To find a relation between the XCP and MSS data, linear regression was done to find the best fitting straight line through the data points. This was done for the data from the three surveys combined. Only MSS data above twice the noise level is used in the regression to remove the MSS data which might be overestimated. The regression was then done over 806 data points. The power law fit states that there is a relation between the two datasets, $K_{\rho_{XCP}} = aK^b_{\rho_{MSS}}$, where a and b are constants. Taking the logarithm of both sides we get $\log_{10}(K_{\rho_{XCP}}) = \log_{10} a + b \log_{10}(K_{\rho_{MSS}})$, which is the linear relationship $y = A + bx$ between two different inputs y and x. Here $A = \log_{10} a$ and b are constants, and describe respectively the interception with the y-axis and the slope of the straight line. The result is shown in figure (4.7) for both power fit scenarios where $a = 1$ or a free variable. For the latter scenario $A = -2.33 \pm 0.24$ and $b = 0.47 \pm 0.04$, where uncertainty is the standard error. A means that the MSS data must be multiplied $10^{-2.33}$ to resemble the XCP data. Also the linear correlation coefficient here is 0.6. For the scenario, when the intercept is forced to zero, i.e. $A = 0$, $a = 1$, we obtain $b = 0.90$ within 95% confidence

limits of ±0.02. For the perfect one to one relation, this should be unity.

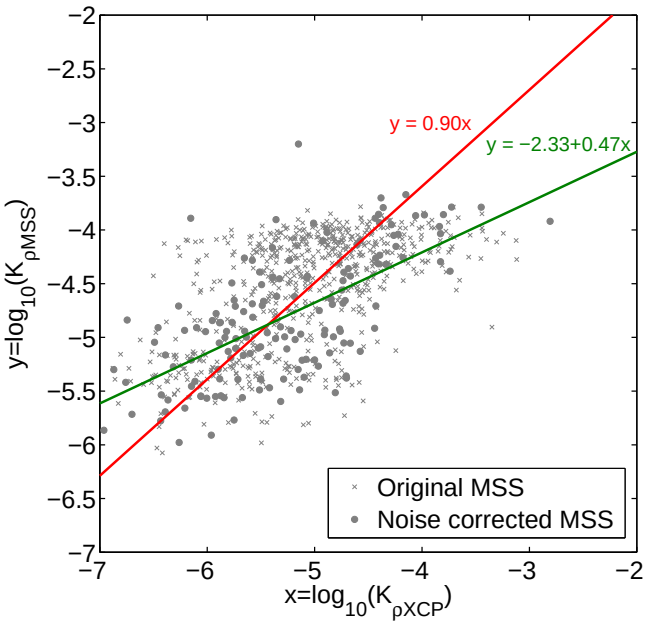

Figure 4.7: Scatterplot for the XCP and MSS data used in the regression. Grey dots show the data points when the MSS data are above the noise level, grey crosses show the data near the noise level and the green and red line show respectively the regression result with and without the interception on the y-axis.

Further, trying to estimate an uncertainty in the XCP eddy diffusivity obtained from the internal-wave parameterization we compute the fractional error $|K_{\rho MSS} - K_{\rho XCP}|/K_{\rho MSS}$. The fractional error is noisy as can be expected from the scatter in figure (4.7). A meaningful result, however, is obtained looking at the histogram of error. Because, for example, within a factor of 2 of a variable x spans $0.5x$ to $2x$, we use the inverse of fractional error less then unity in the histogram. The result is shown in figure (4.8) and show the frequency histogram of the fractional error relative to MSS observations for both fine scale parameterizations. This shows that the fractional error, mean and standard deviation is reduced when using the Kunze et al. (2006) parameterization. The average value for the corrected XCP data is 2.6 with a mean standard deviation of ±3.6 and we assign the uncertainty in the XCP eddy diffusivity estimate to be within a factor of 5-6.

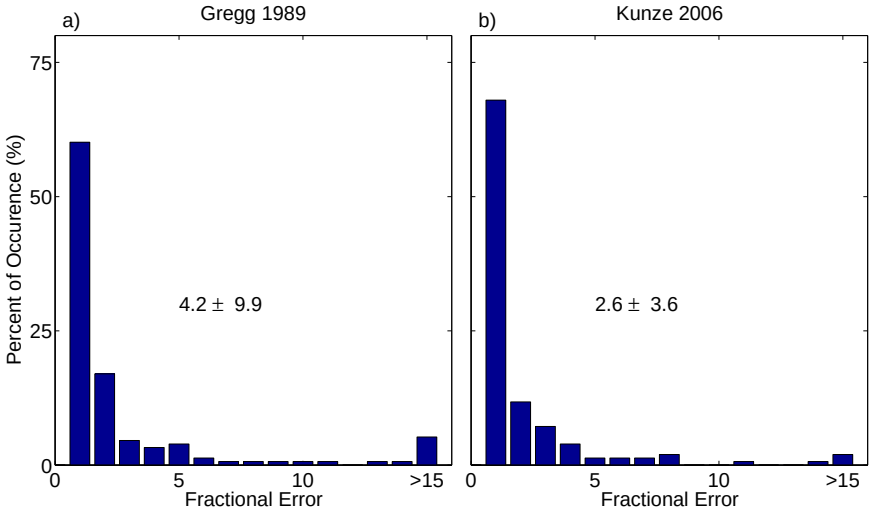

Figure 4.8: The frequency histogram for a) the original XCP data and b) the corrected XCP data. The mean and one standard deviation are indicated on the figure.

4.2 Comparison of XCP drops done at the same location and similar in time

Several XCP deployments were done at the same time and same location. By applying the identical processing and parameterization, we can infer the accuracy of K_ρ estimates. Comparisons can be seen in figure (4.9) to (4.12), which shows velocity profiles, spectra and the eddy diffusivity. Information of the XCP deployments used is given in table (4.1).

Because the XCP profiles measure the relative velocity components, the velocity profiles (figure (4.9) to (4.12)) show the XCP measured velocity after removing the depth-averaged velocity. The velocity profiles from the XCP deployments in each figure show no big changes in the velocity fields. The corresponding velocity spectra over the top 600 m are also similar, with comparable spectral levels and shape, identical within the 95% confidence limits. The eddy diffusivity profiles are similar, with only a difference in the fluctuations.

It can be noted that the SCICEX 1993 derived spectra show a higher energy level and have a different spectral shape compared with the spectra from other surveys. The SCICEX 1993 velocity is also higher and the fluctuations bigger. And after the error screening, SCICEX 1993 survey results in scarce number of eddy diffusivity values.

Table 4.1: The XCP drops used in the figures 4.9 to 4.12

Survey	Drop	Date	Time	Lat	Lon
SCICEX 1993	14	03.9.1993	04:06:42	80N 00.30	179E 56.60
SCICEX 1993	15	03.9.1993	04:19:52	80N 00.30	179E 56.60
Borneo 2008	18	25.4.2008	18:00:00	89N 14.40	90W 24.10
Borneo 2008	19	25.4.2008	18:40:00	89N 14.40	90W 24.10
NPEO 2010	10	23.4.2010	11:15:00	89N 59.50	7W 04.00
NPEO 2010	11	23.4.2010	12:40:00	89N 59.50	7W 04.00
NPEO 2010	17	25.4.2010	14:38:00	89N 01.10	178W 39.90
NPEO 2010	18	25.4.2010	14:53:00	89N 01.10	178W 39.90
NPEO 2010	19	25.4.2010	15:20:00	89N 01.10	178W 39.90

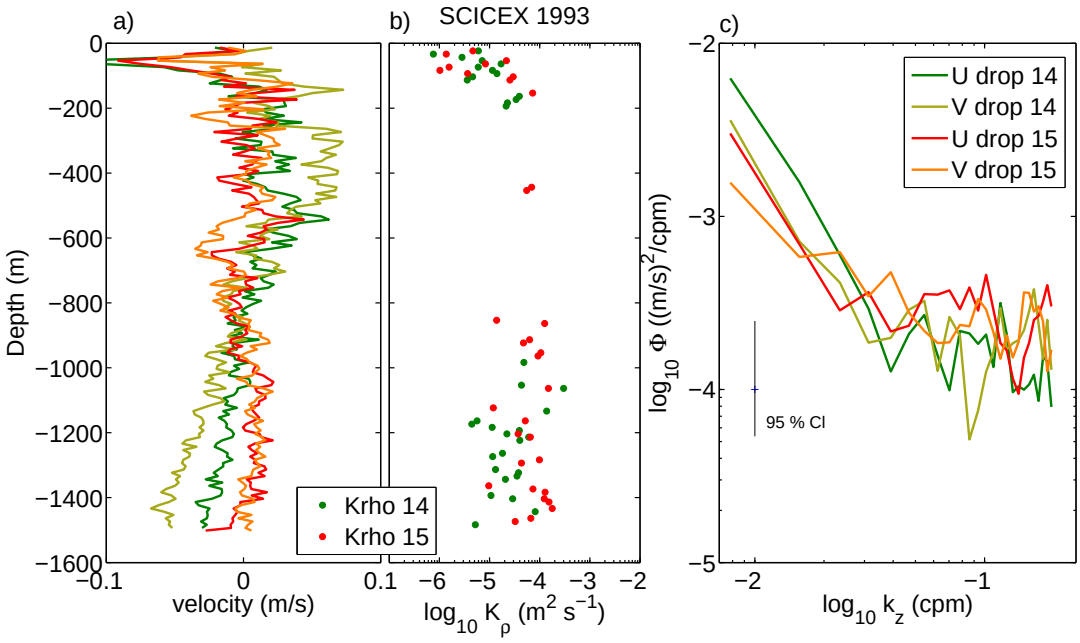

Figure 4.9: a) The XCP velocity profiles, b) the velocity spectra and c) the XCP derived eddy diffusivity. Shear spectra are truncated at $k_z \geq 0.2$ cpm where filtering attenuates the spectra.

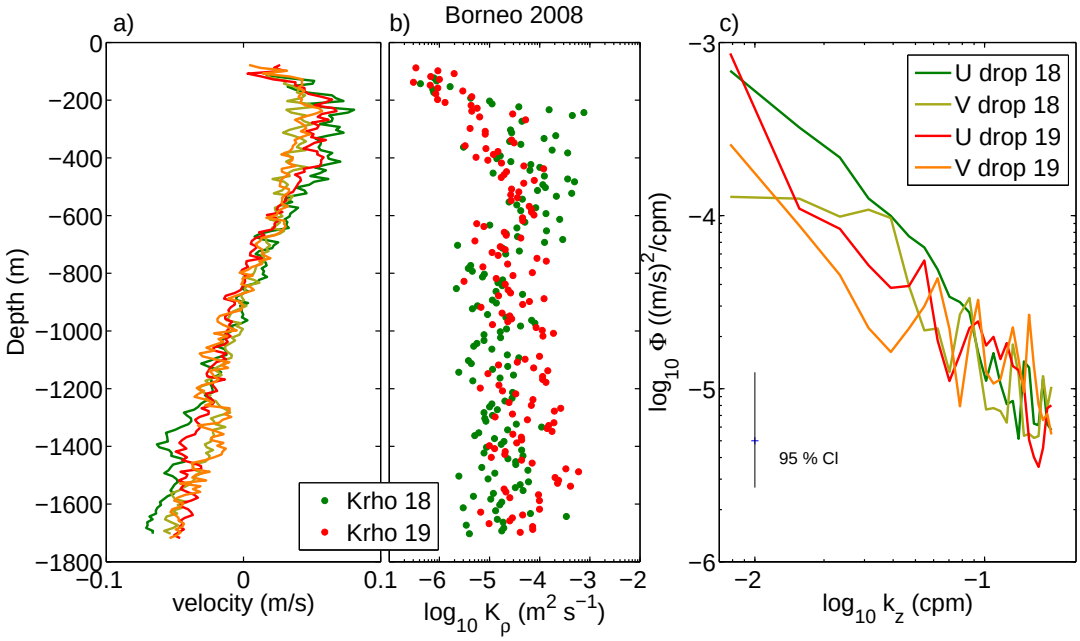

Figure 4.10: Same as figure (4.9) but for Borno 2008.

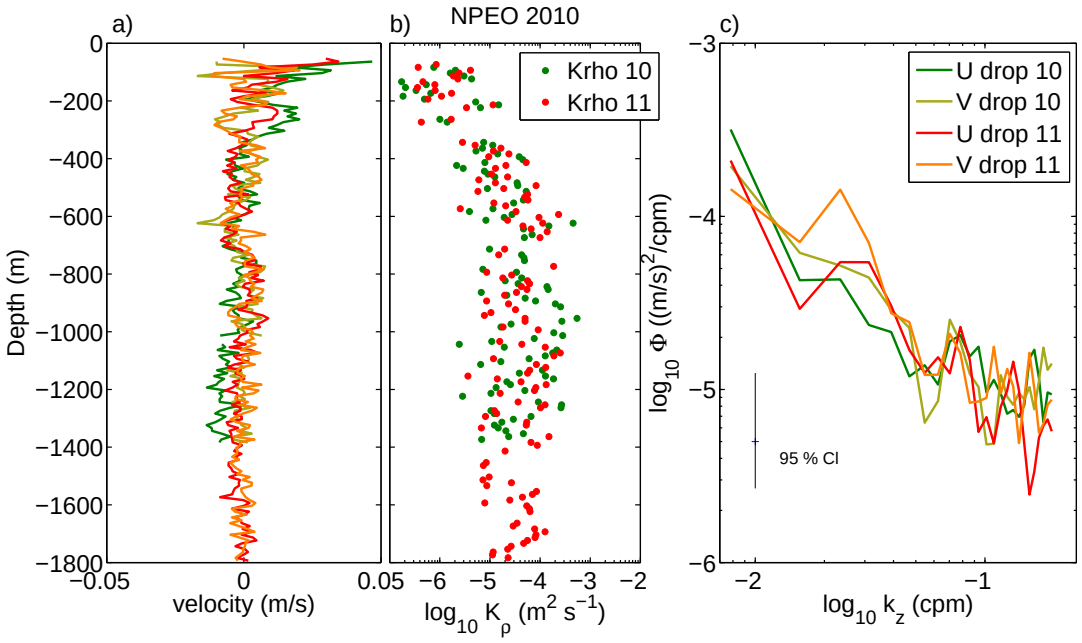

Figure 4.11: Same as figure (4.9) but for NPEO2010 drops 10 and 11.

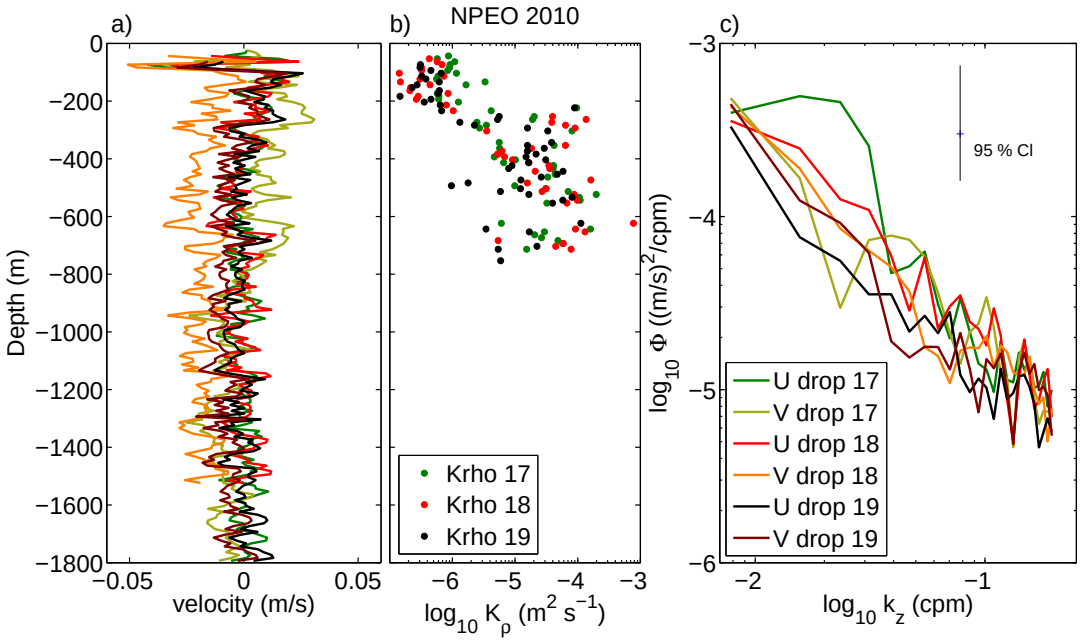

Figure 4.12: Same as figure (4.9) but for NPEO2010 drops 17,18 and 19.

Figure (4.13) shows a scatter plot of all the pairs (drop number 17 and 18 from figure (4.12)) of eddy diffusivity. This shows that Borneo 2008 drops 19 and 20, and NPEO 2010 drops 10 and 11 have the largest deviations from the different drops. However, these are also the drops with the most number of eddy diffusivity values retained after the error screening.

The eddy diffusivity data were then averaged over 10 data points (10 m vertical length), and all profiles pairs are combined for linear regression. This was done the same way as in section (4.1). When the intercept is set to zero, the regression line attains nearly a slope of unity, with $b = 0.98$ within 95% confidence limits of ± 0.02. With the interception, $a = -1.94 \pm 0.26$ and $b = 0.59 \pm 0.05$. The correlation coefficient $r = 0.57$. Overall $y = (0.98 \pm 0.02)x$ leads us to conclude that the eddy diffusivity inferred from pairs of XCPs deployed at the same location and same time agree very well, lending credit on the model and the instrument. Given the scatter in figure (4.14), however, the accuracy is probably comparable to the uncertainty upto one order of magnitude.

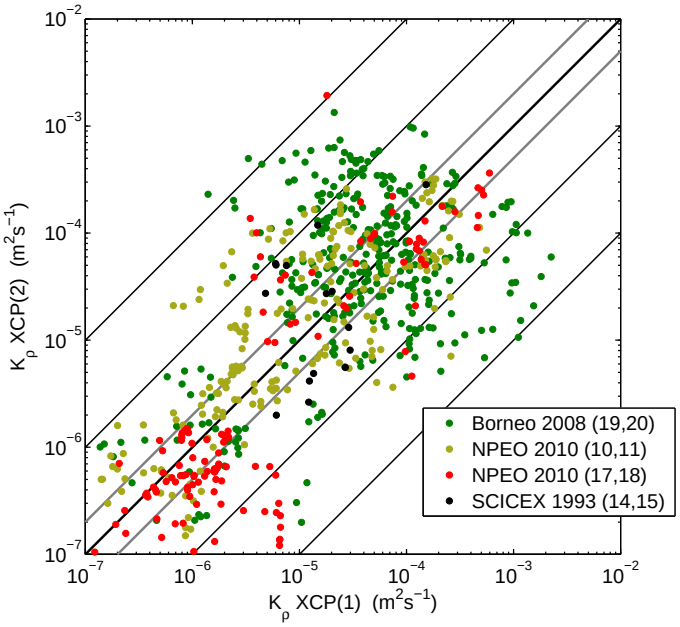

Figure 4.13: Scatter plot of the different pairs used in the analysis. The drop numbers can be found in the legend. Diagonal lines envelope a factor of 2, 10 and 100.

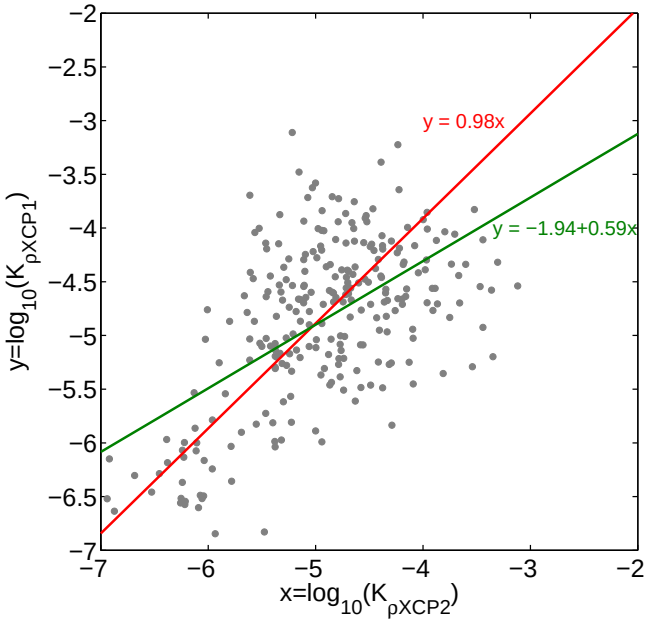

Figure 4.14: Scatterplot for all the XCP data used in the regression. Grey dots show the data points used and the green and red line show respectively the regression result with and without the interception on the y-axis.

4.3 Topographic variation

The XCP deployments were divided into three categories of different topography: continental shelf and slope areas (slope), areas over ridges (ridge), and the part of the Arctic Ocean that is not influenced by topography (abyss). There is almost no data from deployments done at total water depths less than 500 m, so the shelves are undersampled. Table (4.2) gives information about the XCP drops used in each category, figure (4.15) shows the different locations of the XCP drops and figures (4.16) and (4.17) give an illustration of the eddy diffusivity results.

Table 4.2: The XCP drops used in figures 4.16 to 4.18

Location	Survey	Drop
Abyss	SCICEX 1993	4-7, 12-13, 22-23
	Louis 2007	5,8
	Borneo 2007	3-6
	Borneo 2008	1-9, 11-14
	NPEO 2007	3
	NPEO 2008	2-3, 8
	NPEO 2010	1,5, 8-15
	SY 2010	4
Slope	SCICEX 1993	17-21
	Louis 2007	1, 4, 7
	Yermak 2007	1-2, 4, 6, 8, 12-13, 15-17
	NPEO 2008	1, 4
	SY 2007	2
	SY 2010	2
Ridge	SCICEX 1993	3, 8-9, 11, 14-16, 24, 26 28-30
	SY 2007	3
	Borneo 2008	15-19
	NPEO 2007	2, 5-6
	NPEO 2008	6-7, 9-10
	NPEO 2010	6-7, 17-19

Figure (4.16) shows the diffusivity profiles for the three different categories, with the individual XCP deployments at 50 m resolution and the corresponding mean profiles, where the averaging is done over 10 data points and the vertical resolution is 5 m. Figure (4.17) compares the mean profiles from each category. The mean value of eddy diffusivity from the different categories calculated in the top 300 m of the water column, and from 300 m to the bottom are summarized in table (4.3). This shows that the variability in the upper 300 m is not significant, i.e, much less than the factor of 5-6 uncertainty. In the deeper layers the eddy diffusivity from slope and ridge areas is higher and similar in value, with the abyss being a factor of two lower. This is again less than the large uncertainty inherent in the XCP-derived eddy diffusivity estimates, however, suggests stronger mixing

above topography compared to the abyss. It should be noted that the abyssal average is done over 42 profiles, the ridge average over 30 profiles and the slope average over 22 profiles, where most profiles reach to $\sim$ 1000 m.

Table 4.3: The mean XCP eddy diffusivity from the top 300 m and the depth below 300m.

Location	Upper 300 m	400 -1800 m
Abyss	1.4 10^{-5}	2.8 10^{-5}
Slope	1.8 10^{-5}	4.7 10^{-5}
Ridge	2.0 10^{-5}	4.7 10^{-5}

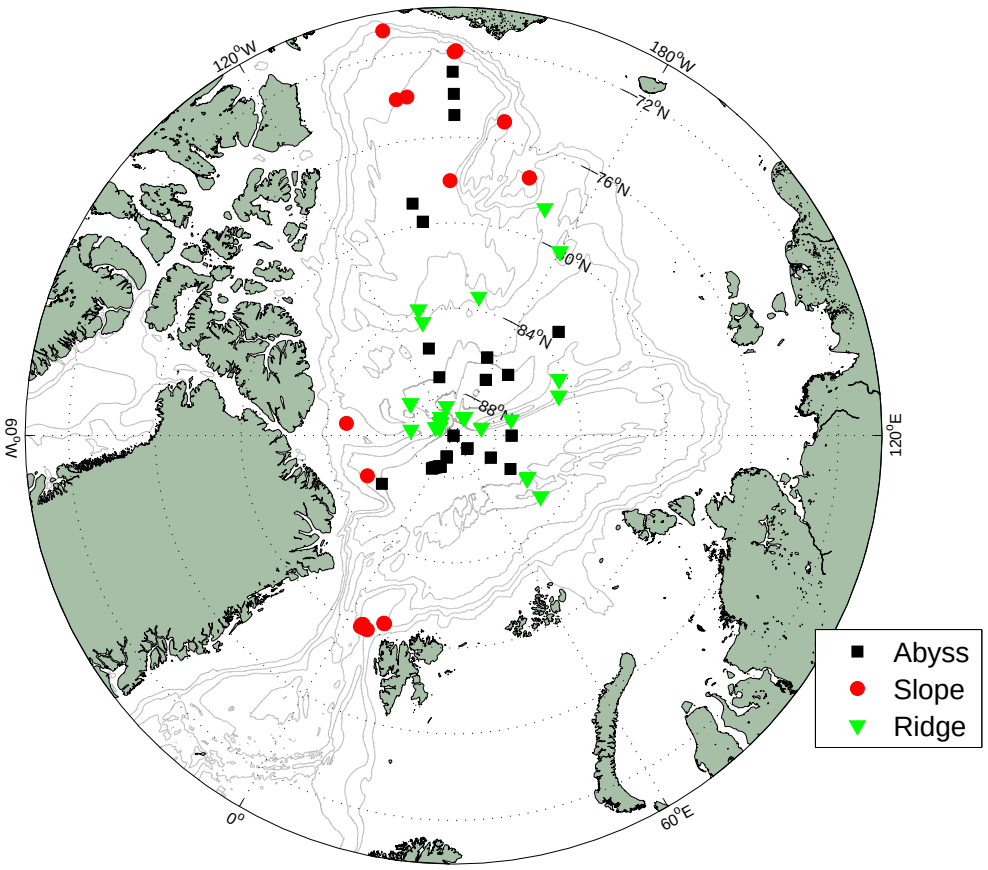

Figure 4.15: A map showing the drops used for the different topographic categories marked with different color and symbol.

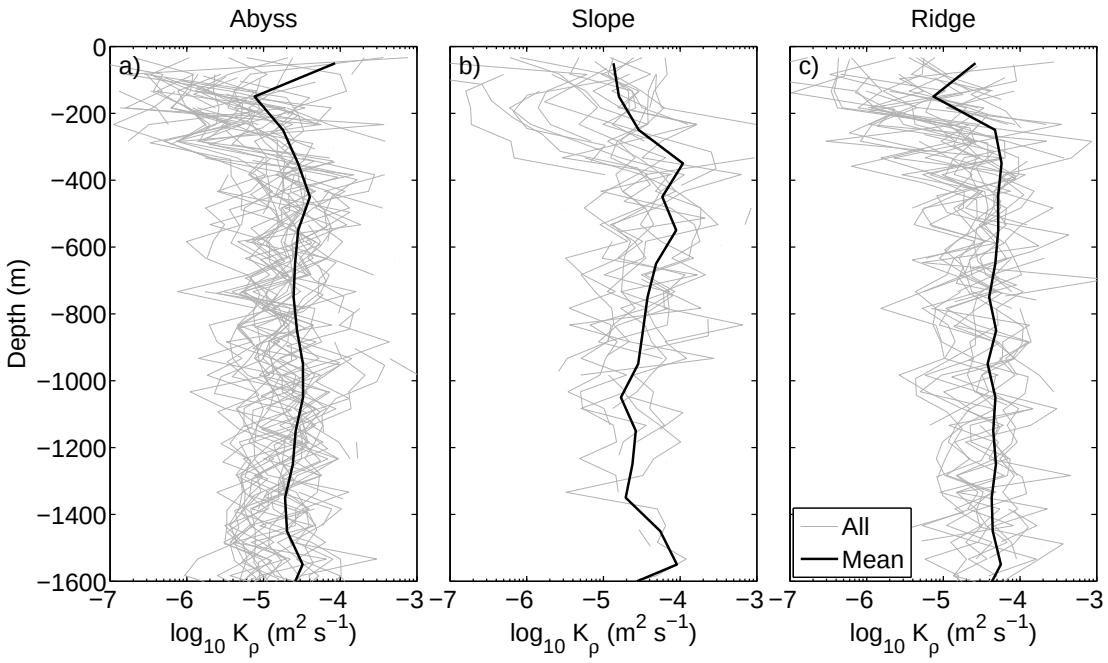

Figure 4.16: Averaged eddy diffusivity profiles for a) the measurements done away from topography, b) over shelf areas and c) done over ridges. Grey lines show the individual XCP drops and black lines show the average diffusivity from the XCP drops.

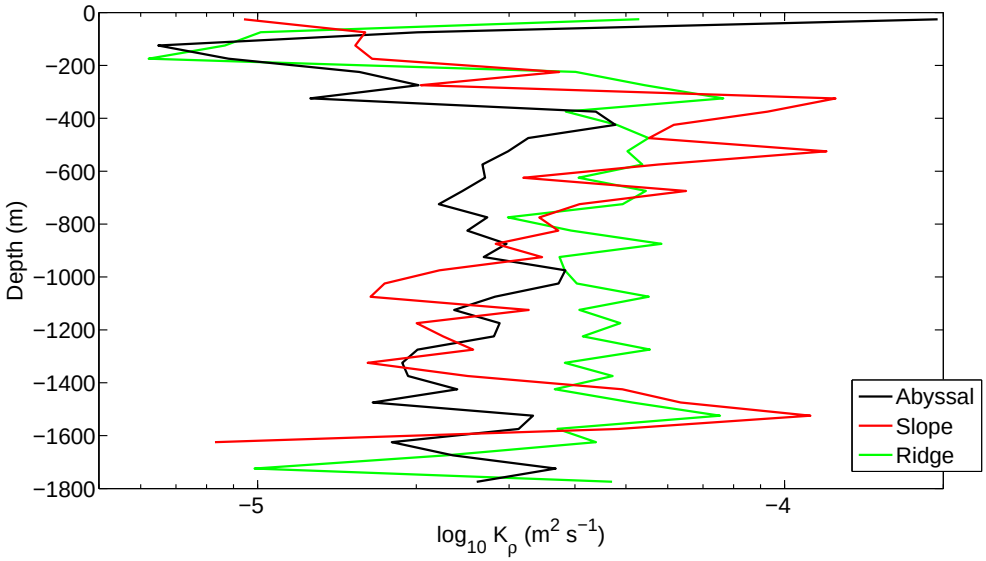

Figure 4.17: The average eddy diffusivity profiles done over away from topography (black line), over shelf and slope areas (red line) and over ridges (green line)

4.4 Temporal variability

The temporal variability is investigated by comparing the data collected during SCICEX 1993 with the rest of the surveys. Comparison of the eddy diffusivity profiles can be seen in figure (4.18) and of the velocity spectra in figures (4.19) and (4.20).

Figure (4.18) shows that the inferred eddy diffusivity from SCICEX 1993 is consistently higher than that from the more recent data. After the error screening, there is almost no data left for the SCICEX 1993 data below 400 m and the average over the deeper parts hence includes only few profiles. Also the velocity profiles from SCICEX 1993 show a higher velocity variance with larger and more frequent fluctuations than from the rest of the surveys.

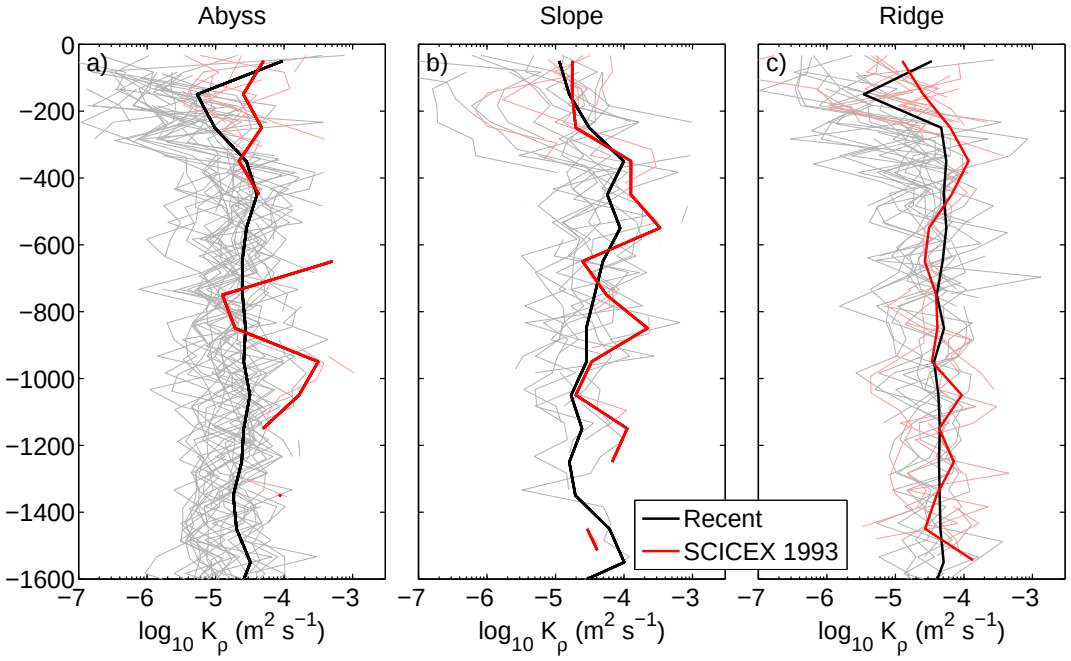

Figure 4.18: Averaged eddy diffusivity profiles as in figure 4.16 for a) abyssal, b) slope and c) ridge areas. Thin red lines show the individual XCP drops collected during SCICEX 1993, the thick red line gives the mean profile, grey lines show the measurements done after SCICEX 1993 and the black line shows the mean.

The energy spectra in figures (4.19) and (4.20) show higher energy level for the SCICEX 1993 data compared with the other surveys. The SCICEX 1993 spectra also have a white slope at wavenumbers greater than 2×10^{-2} cpm, which suggests that the data at vertical scales smaller than 50 m are dominated by noise.

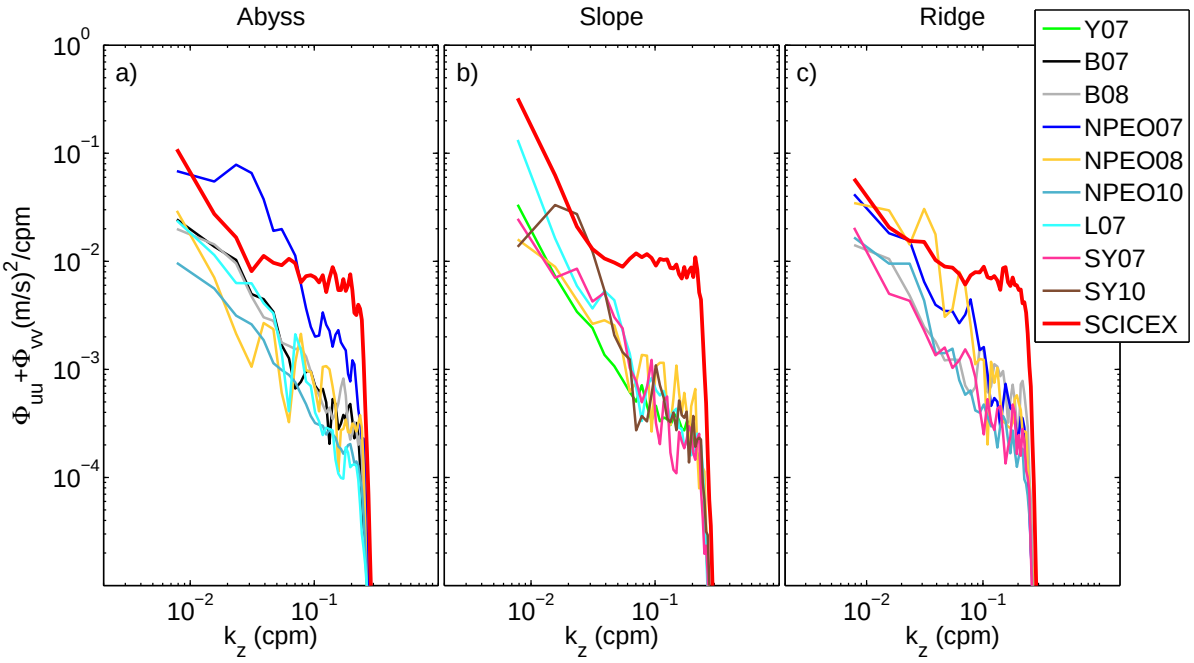

Figure 4.19: Upper 300 m mean energy spectra over each survey for a) abyssal, b) slope and c) ridge. Attenuation after 0.2 cpm is due to filtering. A lack of corresponding spectrum means no station or not sufficient length of data to calculate a spectrum.

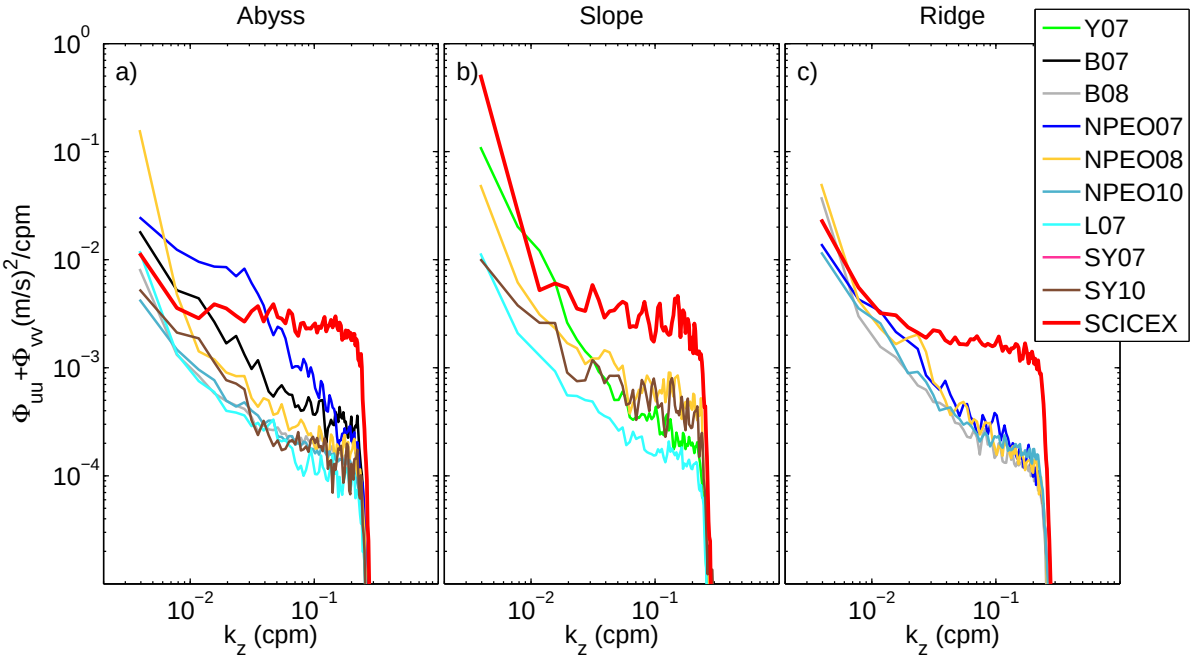

Figure 4.20: Same as figure (4.19), but for the lower 400-1500 m.

Chapter 5

Discussion

5.1 Skill of the finescale parameterization

The available microstructure measurements using the MSS made it possible to compare the parameterization used to infer eddy diffusivity with direct observations. The corresponding individual profiles agree reasonably well. However the mean profiles obtained from the MSS show higher eddy diffusivity values than the XCP inferred values below the cold halocline layer. The MSS profiles have a noise level in dissipation rate ε of $\sim 10^{-9}$ Wkg^{-1} which is large in quiescent Arctic waters (Fer 2009). The dissipation profiles below the cold halocline layer are at the noise level leading to the eddy diffusivity being significantly overestimated below the pycnocline.

Previous work have tested the internal wave parameterization at lower latitudes, where the internal wave field is consistent with the Garrett and Munk internal wave field. The general skill of the internal wave parameterization is found to agree with observations to within a factor of 2 (Polzin et al. 1995, Gregg 1989). In the Arctic, the conclusion is not so robust, mainly due to the low signal level. The dissipation rate observations over the Yermak Plateau, where significant internal wave energy is observed, could not be captured by the Gregg (1989) parameterization (Wijesekera et al. 1993). They showed that strain was a better proxy than the shear for the internal wave energy for this particular region. In a more recent survey, Fer et al. (2010), it was showed that observed dissipation profiles were captured after accounting for the shear-strain ratio. However, the direct dissipation measurements lowest detection limits is not sufficient to resolve the quiet Arctic interior, and because the Arctic Ocean is a region that deviates from the GM conditions, we included the strain and latitude dependence to improve the parameterization.

The shear-strain ratio R_ω is, however, uncertain. We imposed $R_\omega = 11$ inferred from

the Yermak Plateau (Fer et al. 2010) to the data. When latitude and R_ω corrections is included, the regression against MSS observations showed that $K_{\rho XCP} = K^b_{\rho MSS}$ gives a marginally better fit for the XCP diffusivity obtained using Gregg (1989) parameterization, with $b = 0.93$, compared to the corrected data with $b = 0.90$. However, the Kunze et al. (2006) parameterization is still preferred since the latitude and shear-strain ratio are much different than the mid-latitude derived GM model spectrum used in the internal wave parameterization. Also the fractional error estimate shows that the Gregg (1989) version leads to a larger error and scatter. The fractional error estimate also leads us to conclude on the general skill of the internal wave parameterization for the Arctic Ocean conditions; the estimates of eddy diffusivity agree with the observations to within a factor of 5-6.

Turbulence in the ocean interior is assumed mainly to be driven by breaking internal waves, and the Gregg (1989) parameterization is valid for turbulence generated by internal waves only. But in the quiescent Arctic Ocean other mixing mechanisms can become important, for example double diffusion. As these processes are not included in the model inferring the diapycnal eddy diffusivity, this can lead to wrong results, and underestimate the mixing at regions of low internal wave energy dissipation. This also makes the larger estimates in deviation from observations of a factor of 5-6 compared to the mid-latitude factor of 2 more reasonable.

5.2 Reliability of the XCP measurements

Comparing deployments done at the same location and similar in time should provide a result close in magnitude. However since the measured quantity is turbulence, which is intermittent, some variation is expected. The velocity energy spectra and eddy diffusivity show no big variation from the different drops. The spectral values lay within the 95% confidence limits. Linear regression shows that the best fitting line is close to unit slope. This leads us to conclude that the agreement between the eddy diffusivity inferred from pairs of XCPs deployed at the same location and same time is very well, supporting both the instrument and the model. However, the eddy diffusivity profiles from the corresponding XCP deployments show some deviation. The accuracy is probably comparable to the uncertainty and concluded to be one order of magnitude.

D'Asaro & Morehead (1991) used two XCPs deployed about 1 m and 10 s apart to estimate the noise level and errors in the depth. First to get an estimate of the noise level

the average of 45 horizontal velocity spectrum provided by the XCP were done. This showed that the spectrum became white after ∼0.2 cpm. Then the difference in velocity between the two XCPs were used to calculate the spectra, which was white at about the same spectral energy level as the averaged spectrum. They therefore suggest that white slope was a good model for the XCP noise. We also find the white slope in our data to be consistent with noise. An example is seen in figure (3.16) for a profile with low signal to noise ratio. This is similar to the white slope observed for the SCICEX 1993 data, which is why we suggest that the data at vertical scales smaller than 50 m in SCICEX 1993 are dominated by noise.

The error in depth was investigated comparing the velocity features of the two XCPs deployed nearly simultaneously, which showed a depth difference of 2 m (D'Asaro & Morehead 1991). They suggested that this deviation is due to difference in the launch procedure. We compared the temperature profiles with the ones provided by the CTD or MSS. In our study we adjusted the depth of the XCP profiles with a vertical constant to match the observed temperature profiles.

5.3 XCP performance at high latitudes

The use of XCPs are more common at mid-latitudes, and have been used in measurements of internal wave shear (e.g. Kunze et al. (2002)). But they have also been used successfully in the Arctic Ocean (e.g. D'Asaro & Morison (1992), Boyd & D'Asaro (1994)). The XCP uses the vertical component of the magnetic field for the velocity measurements, and at high latitudes this is large. But the horizontal magnetic field is weak, approaching zero at the magnetic north pole. This can affect the velocity data as it is difficult to get a signal from the compass coil and can result in errors in the velocity direction. Because of this, the APL software used for the processing in the Arctic includes some changes to compensate. These changes include reducing the band-width for the compass signal and also reducing the threshold signal level which the software uses to determine that a drop has begun. Since the depth of the profile is determined by the fall rate, it is important to get the correct start time to infer accurate depth calculations. At mid-latitude these corrections can lead to, for example, the acceptance of a false start of a drop.

In section (4.1) the eddy diffusivity inferred from the XCP velocity was compared with directly measured MSS eddy diffusivity. This gives a good result and indicates that the XCP is capable to measure the correct velocity shear also at high latitudes. However,

many of the XCP deployments did not result in usable data, as it did not return any velocity data at all, or the eddy diffusivity data were removed after the error screening. The magnetic north pole was located at approximately 82.7°N and 114.4°W in 2005. Looking at the SY 2007 and 2010 stations, which are located closest to the geomagnetic north pole, only 3 of 7 deployments returned usable data for providing an eddy diffusivity profile. A possible reason for the lack of data can be caused by problems due to the proximity to the magnetic north pole. Sanford et al. (1993) used XCP deployments up to a magnetic latitude of 85°N, but did not experience problems due to the weak magnetic field. But there has been observed cases where the adjustments in the software were insufficient to resolve a profile when deployed too close to the Magnetic Pole (Roger Andersen, 2011, personal communication). D'Asaro & Morehead (1991) also discarded 4 XCP profiles suspecting that variations in velocity were due to geomagnetic field fluctuations.

5.4 Mixing over rough topography

The deep Arctic Ocean away from topography is a quiescent environment with weak turbulent mixing. This weak mixing is critical for the maintenance of the cold halocline layer (Fer 2009) and the overlaying ice. Rainville & Woodgate (2009) find large internal waves, enhanced vertical shear and mixing tightly related to the absence of sea ice. With the present ice cover, mixing in the Arctic is primarily along the perimeters, boundaries and over rough topography (D'Asaro & Morison 1992, Sirevaag & Fer 2009, Fer et al. 2010). The tidal velocities over most of the Arctic Ocean are sufficient to generate internal waves over these topographic features, and the bottom mixing is of largest contributor to the deep mixing in the Arctic Ocean.

The mean values for the different topographic categories show no difference within the measurement uncertainty for the top 300 m. However, it is in the ocean interior and bottom the mixing due to internal waves is important, and therefore it is in the deeper layers the difference is of importance. The comparison shows that the eddy diffusivity is a factor of two lower for the abyss than for the other categories. Also when the SCICEX 1993 data, which are likely contaminated by noise and overestimate the eddy diffusivity, are excluded, the diffusivity values is identical to within 2%. The difference in eddy diffusivity from the different topographic categories is within the factor of 5 uncertainty and therefore not conclusive, but suggests larger mixing rates over topographic features. However, the eddy diffusivity obtained for the abyss is a factor of 10 larger than what is expected for the calm interior of the Arctic Ocean. The reason for this can be that

the Osborn (1980) model can not be used for this data as it is only valid for stratified turbulence, as $K_\rho \propto N^{-2}$. In the ocean interior the low stratification can hence lead to unrealistically large eddy diffusivity. However the error screening should have removed the portions of XCP profiles associated with weak stratification. It is also likely that the mixing efficiency of 20% used in the Osborn model is too large for weak turbulence levels.

Another possible reason for the high eddy diffusivity values can be the white slope observed in energy spectra of profiles with low signal to noise ratio. This energy variance at the scales of interest (10 m) is higher than what is expected of internal wave dissipation and will result in higher eddy diffusivity for these profiles. This is not accounted for in this analysis.

There is also a difference in the number of deployments used in the different topographic categories, with the abyss being better sampled than the others. The shelf regions included very few profiles and were therefore combined with slope areas. Because XCPs are expensive they are mostly deployed in deep waters, which result in undersampling over the shelves.

5.5 Temporal variability

One of the intentions of this study was to investigate whether the presence of the ice cover in the Arctic Ocean and its significant retreat in recent years had implications on the internal wave field. The energy levels are expected to be lower compared with ice free areas. For this reason the SCICEX 1993 dataset was of particular interest because of its potential for comparison of eddy diffusivity with the data from 2007 and 2008; a record minimum in the summer extent of the Arctic sea ice cover was observed in September 2007 (Perovich et al. 2008). However, after the error screening, the remaining eddy diffusivity data from this survey is scarce. The velocity profiles significantly differ when compared with the velocity profiles from the rest of the surveys; the fluctuations and the magnitude are larger. The mean SCICEX 1993 energy spectra in figures (4.19) and (4.20) show a white slope at wavenumbers greater than 2×10^{-2} cpm, which suggests that the noise contaminates the shear signal at wavelenghts less than 50 m. Hence it can not be concluded about the temporal variability, as the SCICEX 1993 XCP data are not suitable for finescale parameterization to infer vertical mixing in the Arctic Ocean.

A possible reason for the difference in the SCICEX 1993 data compared with more

recent data, can be the use of an older version of the instrument, which has improved since 1993. However XCPs have successfully been used before 1993 in the Arctic (e.g., D'Asaro & Morison (1992)) and produced reasonable estimates of the eddy diffusivity through the Gregg (1989) parameterization.

Because of possible errors in the XCP measurements, the deployments should be done away from sources capable of disturbing the magnetic field. For this reason XCP deployments from ships are normally done two ship lengths away. There is a 40 s delay before the XCP is released from the buoy at the surface to make this possible (i.e. the ship can steam away from the XCP before the profile has started). The magnetic field of the vessel is then not a problem. This is also true for the deployments done from the sea ice which are away from ships or research vessels. However, what was done differently during SCICEX 1993, and might be a possible explanation for the relatively noisy velocity profiles, might be the fact that these deployments were done during a submarine cruise. The submarine could have influenced the magnetic field and hence also the velocity measurements, although the deployments were made 50∼100 m from the submarine (James Morison, 2011, personal communication).

Using past work, a comparison with older data can be made using the results from D'Asaro & Morison (1992), using XCPs deployed during the the Polarstern Arkis IV/3 summer 1987 over the Nansen Abyssal Plain, Nansen Gakkel Ridge and the Yermak Plateau. In the Nansen Abyssal Plain the largest eddy diffusivity was found to be 7×10^{-6} m^2s^{-1} using the Gregg (1989) parameterization. After correction for latitude variation and the shear-strain ratio this is 4×10^{-6} m^2s^{-1}; using a typical stratification of $N^2 = 10^{-5}$ s^{-2} at 84°N the correction in latitude is ∼1.5 and together with the shear-strain ratio correction of a factor of 0.37 the total correction is $\sim$ 0.6. Our results from the recent surveys lead to an eddy diffusivity of $\sim 2\times10^{-5}$ m^2s^{-1} over the abyss, which is a factor of 5 larger than 1987. This is suggestive of increased mixing rates in the deep Arctic Ocean in the last decade. Over the Nansen Gakkel Ridge and the Yermak Plateau the eddy diffusivity is found to be $\sim 1\times10^{-4}$ m^2s^{-1}, which after the correction of 0.6 is 6×10^{-5} m^2s^{-1} which is almost the same as our estimate over the slope and ridge areas.

Chapter 6

Summary and concluding remarks

In this study recent and historical data sets from different regions of the Arctic Ocean are analysed. This is done using velocity profiles from 127 eXpendable Current Profiler (XCP) deployments from the time period 1993 to 2010, which are all processed identically in the body of this study. The shear profiles of horizontal velocity are used to infer vertical mixing. Using the fine-scale parameterization by Gregg (1989) the dissipation rate of internal wave energy is inferred, which is then used in the Osborn (1980) model to get the eddy diffusivity. The results are compared in relation to topographic variations and temporal variability. Joint microstructure measurements made it possible to compare the XCP derived eddy diffusivity with direct observations to test the applicability of the parameterization.

Appropriate processing of the XCP data is crucial for reliable application of finescale parameterization. Using available software we thoroughly tested the processing and the resulting spectral signature. It is ill-advised to use shear profiles from the manufacturers software package. Instead, 4-m smoothed profiles obtained from the MATLAB software developed at the Applied Physics Laboratory, University of Washington, using segment lengths of 2 m and average the velocity measurements in 1 m vertical bins are recommended.

For some of the XCP deployments, corresponding microstucture profiles are used to compare the XCP derived eddy diffusivity with direct dissipation measurements. The corresponding profiles agree reasonable well, and the parameterization by Kunze et al. (2006) (which compared to the parameterization by Gregg (1989) also include strain and allow a variation in latitude), gives a better result. This revised eddy diffusivity was used in the eddy diffusivity calculations and it is concluded that the XCP derived eddy diffusivity in the Arctic Ocean has an uncertainty to within a factor of 5-6.

Several XCP deployments done at the same time and same location were used to infer an estimate of the accuracy of the eddy diffusivity. Linear regression done on all the corresponding XCP deployments yield significant scatter but a slope close to unity lending support on the use of XCPs and the finescale parameterization. Given the scatter between the measurements, the accuracy is estimated to be comparable to the uncertainty, i.e. within one order of magnitude.

The broad geographical area of XCP deployments made it possible to compare the eddy diffusivity from the abyss, slope and shelf areas and over ridges. This shows that the variability in the upper 300 m is not significant and the results lay within the factor of 5-6 uncertainty. In the deeper layers the eddy diffusivity from slope and ridge areas are comparable in value, and a factor of two higher than the abyss.

Temporal variability was investigated comparing data from 1993 with recent data from 2007 to 2010. But this analysis was inconclusive due to a relatively poor quality data set from 1993. When compared to previously published estimates from 1987 over the Nansen Abyssal Plain, our abyssal estimate are a factor of 5 larger suggesting increased mixing rates in the deep Arctic in the last decade.

As the investigation of temporal variability was not successful using the dataset from 1993, other available measurements can be used to track changes in the internal wave energy due to a changing ice cover. This involves available data from buoys, moorings and Acoustic Doppler Current Profiler (ADCP) measurements. Density and velocity profiles can be used to improve the shear-strain ratio R_ω estimate for the Arctic Ocean, and hence also the internal wave energy estimate using the parameterization by (Kunze et al. (2006)).

Appendix A

The following tables list the XCP deployment details for each survey. The last columns are the horizontal and vertical components of the Earths magnetic field. Rows indicated by grey returned no or bad data.

Table 1: Yermak 2007

XCP S/N	Drop	Date	Time (UTC)	Surface station	Latitude (deg/min)	Longitude (deg/min)	F_h (nT)	$-F_z$ (nT)
06051107	1	23.7.2007	13:47	St1 1	80N 08.58	4E 21.48	6704	54465
06051053	2	23.7.2007	18:30	St1 2	80N 07.90	4E 18.50	6709	54461
07011013	3	23.7.2007	22:08	St1 3	80N 07.06	4E 10.36	6714	54456
06051025	4	24.7.2007	02:40	St1 4	80N 06.07	4E 09.27	6722	54452
06051003	5	24.7.2007	06:43	St1 5	80N 08.49	4E 19.91	6704	54464
06051004	6	24.7.2007	10:10	St1 6	80N 07.29	4E 07.85	6713	54457
07061007	7	27.7.2007	08:59	failed	80N 32.69	9E 85.46	-	-
07031011	8	27.7.2007	10:49	St3 1	80N 33.99	9E 48.90	6517	54648
07061005	9	27.7.2007	14:02	failed	80N 33.85	9E 38.84	-	-
07061003	10	27.7.2007	14:44	St3 2	80N 33.61	9E 36.75	6520	54643
07061002	11	27.7.2007	18:25	St3 3	80N 33.96	9E 46.55	6429	54378
06051109	12	27.7.2007	22:09	St3 4	80N 34.29	9E 46.29	6426	54380
05121030	13	28.7.2007	02:24	St3 5	80N 34.45	9E 36.14	6426	54378
06051108	14	28.7.2007	06:30	St3 6	80N 34.11	9E 47.00	6427	54379
06051089	15	30.7.2007	04:10	F7	79N 59.90	6E 01.40	6680	54188
06051110	16	30.7.2007	06:45	F8	79N 59.70	4E 59.64	6680	54175
07011015	17	30.7.2007	09:17	F9	80N 00.00	3E 58.70	7106	53919

Table 2: Louis 2007

XCP S/N	Drop	Date	Time (UTC)	Latitude (deg/min)	Longitude (deg/min)	F_h (nT)	$-F_z$ (nT)
07011008	1	1.8.2007	10:03	70N 48.89	140W 04.46	7842	57568
07011005	2	4.8.2007	00:32	71N 24.54	152W 02.66	8777	56990
07011009	3	4.8.2007	05:58	71N 33.07	151W 28.90	8629	57041
07021003	4	4.8.2007	16:09	72N 00.09	150W 21.73	8225	57164
07031002	5	5.8.2007	13:02	73N 59.50	150W 01.91	6912	57399
07031004	6	7.8.2007	17:39	75N 39.97	156W 17.86	6326	57380
07031006	7	13.8.2007	15:13	78N 01.31	149W 12.07	4388	57557
07031007	8	16.8.2007	15:05	78N 55.84	139W 58.60	3229	57595
07031024	9	20.8.2007	09:15	75N 45.98	129W 51.98	3900	57915

Table 3: Freshwater Switchyard 2007

XCP S/N	Drop	Date	Time (UTC)	Surface station	Latitude (deg/min)	Longitude (deg/min)	F_h (nT)	$-F_z$ (nT)
05121023	1	2.5.2007	21:53	Lamont 1	88N 08.49	90W 43.39	1856	56558
05121022	2	5.5.2007	21:23	Lamont 3	84N 55.05	66W 27.94	2848	56182
05051020	3	8.5.2007	21:54	Lamont 5	89N 09.60	102W 56.95	1809	56632

Table 4: Freshwater Switchyard 2010

XCP S/N	Drop	Date	Time (UTC)	Surface station	Latitude (deg/min)	Longitude (deg/min)	F_h (nT)	$-F_z$ (nT)	Declination (E)
5051029	1	08.5.2010	12:15	D10	85N 09.36	45E 44.02	3548	55816	47° 26’
5051007	2	15.5.2010	11:55	H10	85N 31.04	34E 52.96	3711	55758	38° 14’
7031023	3	15.5.2010	14:09	I10	85N 55.42	25E 59.67	3730	55774	30° 43’
5121029	4	15.5.2010	14:09	I10	85N 55.42	25E 59.67	3730	55774	30° 43’
7011017	5	15.5.2010	16:50	J10	86N 54.93	45E 29.89	2975	56069	49° 54’
7021002	6	16.5.2010	11:05	K10	84N 21.93	46E 38.39	3769	55728	47° 14’

Table 5: Borneo 2007

XCP S/N	Drop	Date	Time (UTC)	Latitude (deg/min)	Longitude (deg/min)	F_h (nT)	$-F_z$ (nT)
7011019	1	25.4.2007	06:50	89N 00.56	8E 21.66	2444	56456
7011018	2	25.4.2007	18:40	88N 58.86	10E 14.60	2458	56447
7011020	3	26.4.2007	01:30	88N 57.73	11E 26.77	2464	56443
7011012	4	26.4.2007	06:20	88N 57.00	12E 11.39	2468	56440
7011016	5	26.4.2007	16:13	88N 55.65	12E 42.03	2478	56436
7011011	6	26.4.2007	22:50	88N 54.51	12E 56.11	2486	56432
7011021	7	27.4.2007	05:40	88N 53.62	13E 06.36	2493	56429

Table 6: Borneo 2008

XCP S/N	Drop	Date	Time (UTC)	Station	Depth (m)	Latitude (deg/min)	Longitude (deg/min)	F_h (nT)	$-F_z$ (nT)
08021017	1	18.4.2008	22:05	Borneo	4000	88N 24.82	7E 26.60	2734	56050
08011020	2	19.4.2008	05:50	Borneo	4000	88N 24.50	7E 12.20	2737	56048
08011001	3	19.4.2008	13:55	Borneo	4000	88N 24.09	6E 40.77	2740	56046
08011005	4	19.4.2008	22:15	Borneo	4000	88N 23.75	5E 58.79	2743	56043
08011006	5	20.4.2008	06:10	Borneo	4000	88N 23.43	5E 18.77	2746	56040
08011002	6	20.4.2008	13:50	Borneo	4000	88N 22.81	4E 28.48	2751	56037
08011017	7	20.4.2008	21:55	Borneo	4000	88N 20.93	3E 31.40	2767	56029
08011012	8	21.4.2008	05:50	Borneo	4000	88N 18.82	2E 25.20	2784	56020
08011022	9	21.4.2008	14:00	Borneo	4000	88N 17.36	1E 25.50	2796	56013
08011028	10	21.4.2008	22:25	Borneo	4000	88N 15.87	0E 15.00	2807	56006
08011043	11	22.4.2008	06:00	Borneo	4000	88N 14.50	0W 42.30	2817	56000
08011024	12	22.4.2008	14:00	Borneo	4000	88N 12.43	1W 43.75	2833	55992
08011018	13	22.4.2008	21:40	Borneo	4000	88N 10.25	2W 32.50	2850	55983
0801103	14	23.4.2008	05:50	Borneo	4000	88N 07.87	3W 07.65	2868	55974
08011040	15	25.4.2008	14:50	LR1	2000	88N 57.00	114W 46.00	1658	56355
08011042	16	25.4.2008	15:40	LR1	2000	88N 57.00	114W 36.00	1659	56354
08011046	17	25.4.2008	16:30	LR2	1000	89N 07.20	104W 52.50	1772	56323
08011039	18	25.4.2008	18:00	LR3	2200	89N 14.40	90W 24.10	1890	56289
08011027	19	25.4.2008	18:40	LR3	2200	89N 14.40	90W 24.10	1890	56289

Table 7: NPEO 2007

XCP S/N	Drop	Date	Time (UTC)	Surface station	Latitude (deg/min)	Longitude (deg/min)	F_h (nT)	$-F_z$ (nT)
07031003	1	22.4.2007	03:00	85 90E XCP1	84N 58.72	90E 20.71	2289	57246
07031010	2	23.4.2007	23:04	84 135W XCP2	84N 28.69	134W 42.94	369	57109
07031019	3	24.4.2007	03:07	86 135W XCP3	85N 44.53	134W 08.85	270	56993
07031009	4	28.4.2007	17:58	87 135W XCP4	87N 10.41	136W 11.58	786	56885
07031021	5	28.4.2007	21:55	89 135W XCP5	88N 35.00	136W 02.40	1365	56764
07031001	6	29.4.2007	02:23	89 90E XCP6	89N 03.85	84W 30.37	2037	56706

Table 8: NPEO 2008

XCP S/N	Drop	Date	Time (UTC)	Latitude (deg/min)	Longitude (deg/min)	F_h (nT)	$-F_z$ (nT)
8011044	1	24.3.2008	01:59	74N 02.36	140W 18.67	5866	57638
8021004	2	26.3.2008	21:04	74N 58.69	150W 08.67	6216	57396
8021009	3	27.3.2008	20:54	72N 58.31	149W 51.81	7464	57247
8021008	4	28.3.2008	00:14	72N 03.74	150W 05.27	8076	57130
8021016	5	08.4.2008	16:36	86N 19.56	135E 59.51	940	57223
8021013	6	10.4.2008	20:03	85N 59.27	90E 40.57	2178	56985
8021020	7	11.4.2008	17:58	87N 11.36	135E 19.80	1098	57057
8011011	8	12.4.2008	12:41	86N 53.22	89E 34.19	2142	56847
8011045	9	18.4.2008	15:09	88N 38.52	135E 25.08	1503	56784
8021019	10	18.4.2008	18:20	88N 59.55	178E 49.71	1431	56713

Table 9: NPEO 2010

XCP S/N	Drop	Date	Time (UTC)	Latitude (deg/min)	Longitude (deg/min)	F_h (nT)	$-F_z$ (nT)	Declination (E)
10021031	1	19.4.2010	16:08	89N 06.40	78E 12.38	2077	56620	62° 24'
10021022	2	19.4.2010	20:05	89N 06.40	78E 12.38	2077	56620	62° 24'
10021010	3	19.4.2010	20:05	89N 06.40	78E 12.38	2077	56620	62° 24'
10021027	4	19.4.2010	22:50	89N 06.75	76E 40.58	2086	56615	61° 1'
10021017	5	20.4.2010	06:24	89N 06.13	75E 11.20	2100	56611	59° 35'
10021007	6	22.4.2010	14:30	84N 59.50	84E 59.12	2484	57091	56° 44'
10021003	7	22.4.2010	18:24	85N 59.10	89E 34.40	2197	57021	62° 16'
10021030	8	23.4.2010	11:15	89N 59.50	7W 04.00	1951	56579	- 6° 23'
10021025	9	23.4.2010	12:40	89N 59.50	7W 04.00	1951	56579	- 6° 23'
9091029	10	23.4.2010	16:11	87N 57.38	89E 13.41	2058	56767	68° 49'
10021011	11	23.4.2010	16:11	87N 57.38	89E 13.41	2058	56767	68° 49'
10021006	12	24.4.2010	18:12	86N 58.26	179E 50.27	486	57074	116° 12'
10021028	13	24.4.2010	18:30	86N 58.26	179E 50.27	486	57074	116° 12'
10021024	14	24.4.2010	22:42	86N 00.23	173W 17.20	498	57165	55° 50'
10021002	15	24.4.2010	22:57	86N 00.23	173W 17.20	498	57165	55° 50'
10021004	16	25.4.2010	14:22	89N 01.10	178W 39.90	1430	56753	163° 24'
10021005	17	25.4.2010	14:38	89N 01.10	178W 39.90	1430	56753	163° 24'
10021008	18	25.4.2010	14:53	89N 01.10	178W 39.90	1430	56753	163° 24'
10021026	19	25.4.2010	15:20	89N 01.10	178W 39.90	1430	56753	163° 24'

Table 10: SCICEX 1993

XCP S/N	Drop	Date	Time (UTC)	Surface station	Latitude (deg/min)	Longitude (deg/min)	F_h (nT)	$-F_z$ (nT)	Declination (E)
91051030	1	28.8.1993	07:46:00	2	87N 35.10	142W 39.20	1186	56532	164° 30'
91051033	2	28.8.1993	11:11:00	3	83N 21.90	160W 20.20	2101	56995	43° 37'
91051007	3	28.8.1993	11:51:00	3	83N 21.90	160W 20.20	2101	56995	43° 37'
91051037	4	30.8.1993	15:22:50	4	86N 09.50	168E 02.10	1166	56909	60° 11'
91051020	5	30.8.1993	15:53:00	4	86N 09.50	168E 02.10	1166	56909	60° 11'
91051034	6	31.8.1993	09:00:00	5	87N 15.90	119E 51.90	1688	56717	70° 18'
91051088	7	31.8.1993	09:28:00	5	87N 15.90	119E 51.90	1688	56717	70° 18'
91051008	8	01.9.1993	05:10:00	6	84N 42.30	140E 36.80	1483	57234	28° 41'
91051021	9	01.9.1993	05:25:39	6	84N 42.30	140E 36.80	1483	57234	28° 41'
91051010	10	01.9.1993	15:05:52	7	84N 22.80	148E 02.50	1650	57252	21° 44'
91051036	11	01.9.1993	16:42:00	7	84N 22.80	148E 02.50	1650	57252	21° 44'
91051018	12	02.9.1993	04:17:00	8	83N 03.10	164E 34.20	2535	57262	13° 16'
91051019	13	02.9.1993	04:46:00	8	83N 03.10	164E 34.20	2535	57262	13° 16'
91051005	14	03.9.1993	04:06:42	9	80N 00.30	179E 56.60	4554	57126	13° 37'
91051009	15	03.9.1993	04:19:52	9	80N 00.30	179E 56.60	4554	57126	13° 37'
91051003	16	03.9.1993	18:28:19	10	78N 30.30	171W 52.90	5443	56979	18° 2'
91051002	17	04.9.1993	05:03:00	11	77N 23.10	166W 22.40	6019	56892	21° 23'
91051023	18	04.9.1993	05:21:00	11	77N 23.10	166W 22.40	6019	56892	21° 23'
91051004	19	04.9.1993	20:43:30	12	75N 06.20	159W 13.10	7166	56754	25° 14'
91051012	20	04.9.1993	21:57:00	12	75N 06.20	159W 13.10	7166	56754	25° 14'
91051025	21	06.9.1993	02:12:00	13	73N 59.50	142W 09.30	6352	57380	36° 56'
-	22	07.9.1993	-	14	79N 50.90	141W 49.90	3116	57217	47° 4'
91051035	23	07.9.1993	11:35:12	14	79N 50.90	141W 49.90	3116	57217	47° 4'
91051014	24	08.9.1993	10:16:00	15	83N 50.90	134W 19.70	1006	56862	89° 23'
91051016	25	08.9.1993	17:16:00	15	83N 50.90	134W 19.70	1006	56862	89° 23'
91051031	26	08.9.1993	17:47:00	15	83N 50.90	134W 19.70	1006	56862	89° 23'
91051015	27	09.9.1993	13:03:00	16	84N 55.40	134W 55.40	819	56755	114° 19'
91051017	28	09.9.1993	20:50:20	17	87N 28.20	096W 34.50	1849	56250	- 125° 27'
91051022	29	09.9.1993	21:14:10	17	87 28.2N	096W 34.50	1849	56250	- 125° 27'
91051011	30	10.9.1993	04:22:00	18	87 58.2N	067W 36.80	2408	56059	- 91° 7'
1408	31	10.9.1993	05:37:31	18	87 58.2N	067W 36.80	2408	56059	- 91° 7'

References

Aagaard, K., Coachman, L. K. & Carmack, E. (1981), 'On the halocline of the Arctic Ocean', *Deep-Sea Res.* **28A**, 529–545.

Aagaard, K., Swift, J. H. & Carmack, E. (1985), 'Thermohaline circulation in the Arctic Mediterranean Seas', *J. Geophys. Res.* **90**, 4833–4846.

Baker, M. A. & Gibson, C. H. (1987), 'Sampling turbulence in the stratified ocean: statistical consequences of strong intermittency', *J. Phys. Oceanogr.* **17**, 1817–1836.

Boyd, T. J. & D'Asaro, E. A. (1994), 'Cooling of the West Spitsbergen Current: Wintertime observations west of Svalbard', *J. Geophys. Res.* **99**(C11), 22,597–22,618.

Boyd, T., Steele, M., Muench, R. D. & Gunn, J. (2002), 'Partial recovery of the Arctic Ocean halocline', *Geophys. Res. Lett.* **29**, 10.1029/ 2001GL014047.

Cacchione, D. A., Pratson, L. F. & Ogston, A. S. (2002), 'The shaping of continental slopes by internal tides', *Science* **296**, 724–727.

Cairns, J. & Williams, G. (1976), 'Internal wave observations from a midwater float, Part II', *J. Geophys. Res.* **81**, 1943–1950.

D'Asaro, E. A. & Morehead, M. D. (1991), 'Internal waves and velocity fine structure in the Arctic Ocean', *J. Geophys. Res.* **96**(C7), 12,725ï¿½12,738.

D'Asaro, E. A. & Morison, J. H. (1992), 'Internal waves and mixing in the Arctic Ocean', *Deep-Sea Res.* **39**, S 459–S 484.

Emery, W. & Thomson, R. (1997), *Data Analysis Methods in Physical Oceanography*, Elsevier, ISBN 0-444-50757-4.

Fer, I. (2006), 'Scaling turbulent dissipation in an Arctic fjord', *Deep-Sea Res. II* **53**(1-2), 77–95.

Fer, I. (2009), 'Weak vertical diffusion allows maintenance of cold halocline in the central arctic', *Atmos. Ocean. Sci. Lett.* **2**(3), 148–152.

Fer, I., Skogseth, R. & Geyer, F. (2010), 'Internal Waves and Mixing in the Marginal Ice Zone near the Yermak Plateau', *J. Phys. Oceanogr.* **40**, 1613–1630.

Garrett, C. J. & Munk, W. H. (1972), 'Space-time scales of internal waves', *Geophys. Fluid Dyn.* **3**(1), 225–264.

Garrett, C. J. & Munk, W. H. (1975), 'Space-time scales of internal waves: A progress report', *J. Geophys. Res.* **80**(3), 291–297.

Gregg, M. C. (1989), 'Scaling turbulent dissipation in the thermocline', *J. Geophys. Res.* **94**(C7), 9686–9698.

Gregg, M. C., D'Asaro, A., Shay, T. J. & Larson, N. (1986), 'Observations of persistent mixing and near-inertial internal waves', *J. Phys. Oceanogr.* **16**, 856–884.

Gregg, M. C. & Kunze, E. (1991), 'Shear and strain in Santa Monica Basin', *J. Geophys. Res.* **96**(C9), 16,709–16,719.

Gregg, M. C., Sanford, T. B. & Winkel, D. P. (2003), 'Reduced mixing from the breaking of internal waves in equatorial waters', *Nature* **422**(6931), 513–515.

Kunze, E., Firing, E., Hummon, J. M., Chereskin, T. K. & Thurnherr, A. M. (2006), 'Global abyssal mixing inferred from lowered ADCP shear and CTD strain profiles', *J. Phys. Oceanogr.* **36**(8), 1553–1576.

Kunze, E., Rosenfeld, L. K., Carter, G. S. & Gregg, M. C. (2002), 'Internal waves in Monterey Submarine Canyon', *J. Phys. Oceanogr.* **32**(6), 1890–1913.

Levine, M. D., Paulson, C. A. & Morison, J. H. (1985), 'Internal waves in the Arctic Ocean: Comparison with lower-latitude observations', *J. Phys. Oceanogr.* **15**(6), 800–809.

Maykut, G. A. (1982), 'Large-scale heat exchange and ice production in the central Arctic', *J. Geophys. Res.* **87**, 7971–7984.

Maykut, G. A. & Untersteiner, N. (1971), 'Some results from a time-dependent thermodynamic model of sea ice', *J. Geophys. Res.* **76**, 1550–1575.

Morison, J. H. (1986), 'Internal waves in the Arctic Ocean: A review, Geophysics of Sea Ice, edited by N. Untersteiner, Plenum Press', pp. 1163–1183.

Morison, J. H., Long, C. E. & Levine, M. D. (1985), 'Internal wave dissipation under sea ice', *J. Geophys. Res.* **90**, 11,959–11,966.

Morison, J. H., Steele, M. & Andersen, R. (1998), 'Hydrography of the upper Arctic Ocean measured from the nuclear submarine U.S.S. Pargo', *Deep-Sea Res.* **45**, 15–38.

Munk, W. H. (1981), Internal waves and small-scale processes, *in* B. Warren & C. Wunsch, eds, 'Evolution of Physical Oceanography', The MIT Press, pp. 264–290.

Osborn, T. R. (1980), 'Estimates of the local rate of vertical diffusion from dissipation measurements', *J. Phys. Oceanogr.* **10**(1), 83–89.

Padman, L. (1995), Small-scale physical processes in the Arctic Ocean, *in* W. Smith & J. Grebmeier, eds, 'Arctic oceanography: Marginal ice zones and continental shelves (Antarctic Research Series, Vol. 49)', American Geophysical Union, Washington, D.C.

Perovich, D. K., Richter-Menge, J. A., Jones, K. F. & Light, B. (2008), 'Sunlight, water, and ice: Extreme Arctic sea ice melt during the summer of 2007', *Geophys. Res. Lett.* **35**, L11501.

Pinkel, R. (2005), 'Near-inertial wave propagation in the western Arctic', *J. Phys. Oceanogr.* **35**, 645–665.

Polzin, K. L., Toole, J. M. & Schmitt, R. W. (1995), 'Finescale parameterizations of turbulent dissipation', *J. Phys. Oceanogr.* **25**(3), 306–328.

Rainville, L. & Woodgate, R. A. (2009), 'Observations of internal wave generation in the seasonally ice-free Arctic', *Geophys. Res. Lett.* .

Rudels, B., Anderson, L. G. & Jones, E. P. (1996), 'Formation and evolution of the surface mixed layer and halocline of the Arctic Ocean', *J. Geophys. Res.* **101**, 8807–8821.

Sanford, T. B., D'Asaro, E. A., Kunze, E., Dunlap, J. H., Drever, R. G., Kennelly, M. A., Prater, M. D. & Horgan, M. S. (1993), An XCP Users Guide and Reference Manual, Technical Report APL-UW TR9309, Applied Physics Laboratory, University of Washington, Technical report.

Sanford, T. B., Drever, R. G., Dunlap, J. H. & D'Asaro, E. A. (1982), 'Design, operation and performance of an expendable temperature and velocity profiler (XTVP), APL-UW 8110, Applied Physics Laboratory, Seattle, 164 pp'.

Serreze, M. C., Holland, M. M. & Stroeve, J. (2007), 'Perspectives on the Arctic's shrinking sea-ice cover', *SCIENCE* **315**(5818), 1533–1536.

Sirevaag, A. & Fer, I. (2009), 'Early spring oceanic heat fluxes and mixing observed from drift stations north of Svalbard', *J. Phys. Oceanogr.* p. Accepted.

Steele, M. & Boyd, T. (1998), 'Retreat of cold halocline layer in the Arctic Ocean', *J. Geophys. Res.* **103**, 10491–10435.

Wijesekera, H., Padman, L., Dillon, T., Levine, M., Paulson, C. & Pinkel, R. (1993), 'The application of internal-wave dissipation models to a region of strong mixing', *J. Phys. Oceanogr.* **23**(2), 269–286.

Zhang, J. L. & Steele, M. (2007), 'Effect of vertical mixing on the Atlantic Water layer circulation in the Arctic Ocean', *J. Geophys. Res.* **112**(C4).